LBL-35104
UC-405
Preprint

Lawrence Berkeley Laboratory
UNIVERSITY OF CALIFORNIA

Physics Division

Mathematics Department

Submitted to Journal of Computational Physics

A Deterministic Vortex Sheet Method for Boundary Layer Flow

P.S. Bernard

April 1994

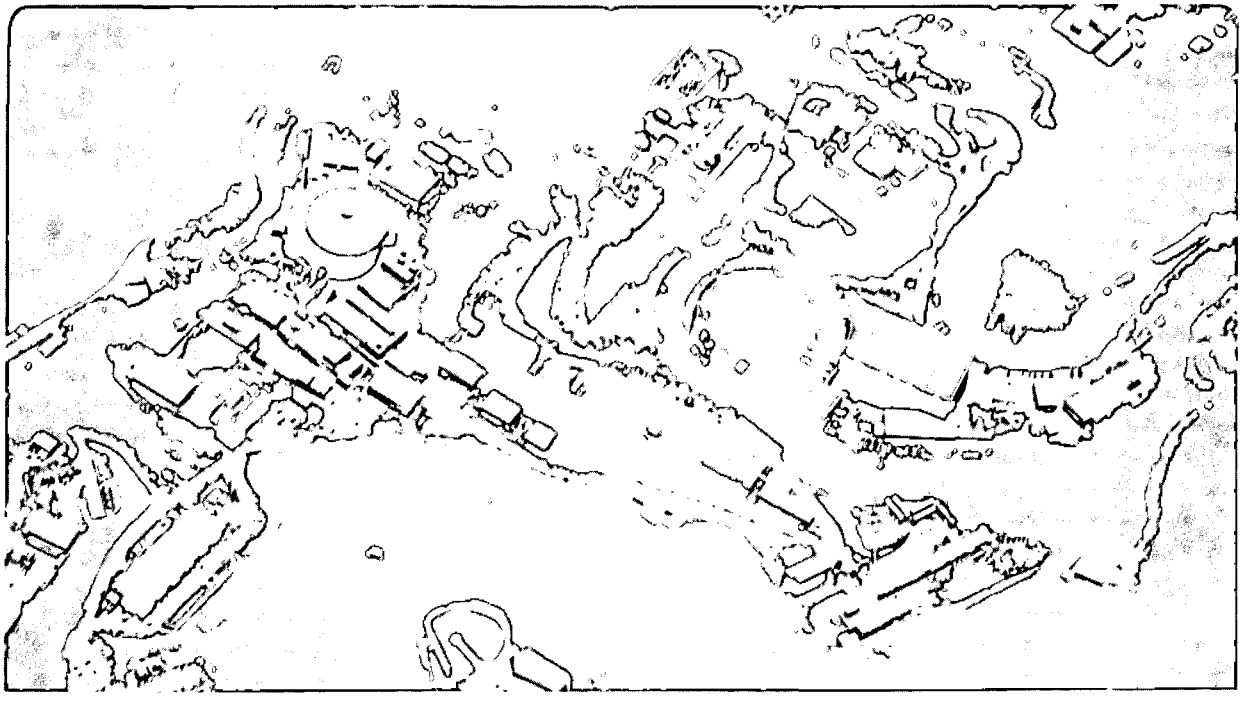

LOAN COPY
Circulates
for 4 weeks
Bldg. 50 Library.
LBL-35104
Copy 2

Prepared for the U.S. Department of Energy under Contract Number DE-AC03-76SF00098

LBL-35104

A DETERMINISTIC VORTEX SHEET METHOD FOR BOUNDARY LAYER FLOW[1]

Peter S. Bernard[2]
Department of Mathematics
and
Lawrence Berkeley Laboratory
University of California
Berkeley, CA 94720

April, 1994

[1]This work was supported in part by ONR Grant N00014-93-10184 and in part by the Applied Mathematical Sciences Subprogram of the Office of Energy Research, U. S. Department of Energy under Contract DE-AC03-76SF00098.

[2]Permanent address: Department of Mechanical Engineering, University of Maryland, College Park, MD 20742

ABSTRACT

A deterministic vortex sheet method is derived for application to boundary layer flows. Diffusive vorticity exchange is through adaptation of a scheme proposed by Fishelov [13] to vortex elements with a sheet-like structure. Special measures are taken to maintain the integrity of the vortex sheet representation at inflow and solid boundaries, including periodically resheeting the flow domain. In calculations of a startup channel flow and zero-pressure gradient and stagnation boundary layers, smooth instantaneous realizations of the velocity field are achieved which closely match exact results.

1. INTRODUCTION

Vortex methods [20] are well suited, in principle, to the numerical treatment of complex, high Reynolds number turbulent flows by virtue of their minimal susceptibility to numerical diffusion and lack of a fixed grid. Recent advances in developing fast vortex methods [1,2,16,17] and the parallel implementation of vortex algorithms on supercomputers [23] have effectively eliminated many past limitations on the number of vortex elements that can be reasonably employed in simulations. It has also become increasingly evident [9] that simulations of three-dimensional turbulence may not require resolution beyond that of the principal energy containing vortical structures. Thus, in analogy to large eddy simulations, the computational requirements of a successful turbulent flow model may be eased by removal of 'subgrid' vortices [8]. The result is that calculations may now be feasible with sufficient scale resolution to provide a physically accurate simulation of three-dimensional turbulent flow [18].

The physics of the turbulent boundary layer is governed by transport deriving from self-replicating quasi-streamwise vortices [4] coupled to strong wall-normal viscous diffusion of spanwise vorticity. To successfully model such flows, vortex element methods must faithfully represent each of these phenomena. A variety of three-dimensional vortex methods have been proposed [20] which may be capable of modeling the inviscid dynamics of coherent vortical structures. Viscous diffusion of vorticity, on the other hand, has tended to be modeled by imposing a random walk on vortex elements [5 - 7, 14, 15]. This has a chaotic influence upon the simulated velocity field which can overwhelm the naturally occurring irregular eddying motion found in real turbulent flow [15]. Consequently, it appears to be essential that a deterministic scheme be used for modeling vorticity diffusion in the context of vortex element simulations of turbulent boundary layer flows.

The focus of this work is the development of a deterministic vortex method capable of providing accurate instantaneous simulations of two-dimensional boundary layers. This will also serve, after suitable generalization, as a methodology for modeling wall-normal vorticity diffusion in the context of a three-dimensional vortex method treatment of turbulent boundary layers. The approach is a non-random reformulation of Chorin's [7] vortex sheet method in which the elements are given a smooth structure such as are now

routinely applied in vortex blob calculations [20]. In particular, fluctuations caused by the velocity discontinuity associated with zero thickness sheets is avoided. Diffusion is only allowed normal to the wall – consistent with the boundary layer assumption – via the exchange process developed by Fishelov [13].

Several alternative approaches toward a deterministic description of diffusion have been introduced in recent years. These include a family of methods in which the Laplacian is approximated by an integral operator evaluated on the vortex elements [10-12, 19, 26] and an approach developed by Russo [21] wherein the diffusion operator is directly estimated on the free Lagrangian grid formed by the vortex particles. In the Fishelov scheme [13], viscous transfer between vortex elements is arranged by applying the diffusion operator to the smoothed vorticity field. As will be seen below, this method is readily adaptable to the geometry of sheets and the presence of a solid boundary, and is perhaps the most natural of the deterministic methods to implement within the context of the current scheme.

Deterministic vortex algorithms require that that part of the flow domain containing the support of the vorticity must be completely covered by vortex elements at all times. For the present scheme this implies that vortex elements near the solid boundary must be allowed to change size in order to prevent the formation of regions free of vortex elements. This has another consequence – in common with other Lagrangian methods [14,21] – that the flow field be periodically regridded or 'resheeted' to restore uniformity to the distribution and size of the elements. An examination of some of the implications of this procedure is given below.

An algorithm for boundary layer simulation via smooth vortex sheets is presented in the next section, followed by an analysis of the kinematics of computing velocities from given positions and intensities of the vortex elements. A treatment of boundaries is then given after which the performance of the scheme is analyzed in the context of several particular flows. These include the transitory development of a channel flow in which the time accuracy of the method is investigated, a zero-pressure gradient Blasius boundary layer and the boundary layer developing downstream of a stagnation point, i.e., the Falkner-Skan similarity solution corresponding to a linearly increasing outer flow velocity [22]. In the last section conclusions are presented.

2. VORTEX SHEET ALGORITHM

The evolution of the vorticity field, $\omega(\mathbf{x}, t)$, in two-dimensional flow is governed by the transport equation

$$\frac{\partial \omega}{\partial t} + \mathbf{u} \cdot \nabla \omega = \frac{1}{R} \nabla^2 \omega \tag{1}$$

where R is the Reynolds number and $\mathbf{u} = (u, v)$ is the velocity field. In the present scheme, approximate solutions to (1) are obtained in the form of collections of N vortex sheets or "tiles" of large aspect ratio l_i/h_i, where $2l_i$ and $2h_i$ are the width and height of the ith tile, respectively. The vortex sheets are assumed to have uniform vorticity, $\omega_i(t)$, and convect with the velocity of their centers – generally without change of size and shape. For most of the sheets, h_i and l_i are assigned common constant values h and l, respectively, equal to the initial dimensions of the vortex element field. The typical vortex sheet representation at the start of a boundary layer calculation is illustrated in Fig. 1. For reasons which will become evident below, sheets at the inflow boundary and close to the wall are permitted to increase in size after each convective step. For these special elements, h_i and l_i are time dependent.

Figure 1 shows a layer of sheets of half thickness arranged along the wall. These elements are kept stationary during the calculation, consistent with the view that they are full sized sheets whose centers are on the wall surface and hence non-moving. The vorticity of these elements is assigned at each time step in such a way as to satisfy the no-slip boundary condition.

The convection term on the left-hand side of (1) is satisfied by having the positions $\mathbf{x}_i(t) = (x_i(t), y_i(t))$ of the vortex sheets obey the kinematic equation

$$\frac{d\mathbf{x}_i}{dt} = \mathbf{u}(\mathbf{x}_i(t), t). \tag{2}$$

For the results presented below, the explicit first order scheme

$$x_i^{n+1} = x_i^n + \Delta t u_i^n \tag{3}$$

$$y_i^{n+1} = y_i^n + \Delta t v_i^n \tag{4}$$

is used to advance the positions of the vortex sheets, where x_i^n and y_i^n are discrete approximations to $x_i(n\Delta t)$ and $y_i(n\Delta t)$, respectively, $u_i^n \approx u(x_i^n, n\Delta t), v_i^n \approx v(x_i^n, n\Delta t)$

and Δt is the time step of the calculation. Some computations were also made using a second order Runge-Kutta approximation to (2), though these did not lead to any noticeable differences in the computed results. This may be due to the limited scope of the applications considered here, e.g., high order approximations to (2) may be of more significance in complex non-steady flows.

To take into account vorticity diffusion in the boundary layer, Eq. (1) may be interpreted in a Lagrangian sense as

$$\frac{d\omega_i}{dt} = \frac{1}{R}(\nabla^2\omega)_i \tag{5}$$

where $(\nabla^2\omega)_i$ denotes evaluation of $\nabla^2\omega$ at the location of the ith vortex. Following the development in Fishelov [13], ω may be convolved with a cut-off function ϕ_δ to obtain the approximate representation

$$\omega \approx \phi_\delta * \omega \tag{6}$$

from which the estimate

$$\nabla^2\omega \approx \nabla^2\phi_\delta * \omega \tag{7}$$

follows. Substituting (7) into (5) and evaluating the convolution integral by summing over the collection of sheets, a basis for a deterministic model of vorticity diffusion is provided. For a first order explicit approximation to the left-hand side of (5) there follows

$$\omega_i^{n+1} = \omega_i^n + \frac{\Delta t}{R}\sum_j \omega_j^n \int_{A_j} \nabla^2\phi_\delta(\mathbf{x}_i - \mathbf{x}')\, d\mathbf{x}' \tag{8}$$

where A_j is the area occupied by the jth vortical element. For the present study, which is limited to planar flow, ϕ_δ is chosen to be the fourth order cut-off function [3]

$$\phi_\delta(x,y) = \frac{1}{2\pi\delta^2}\left(4e^{-\frac{r^2}{\delta^2}} - e^{-\frac{r^2}{2\delta^2}}\right) \tag{9}$$

in which $r^2 = x^2 + y^2$ and δ is the cutoff parameter.

For unbounded flows Fishelov [13] showed that (8) may be made the basis for a consistent approximation to (5). However, in the presence of boundaries, the radially symmetric structure of ϕ_δ means that part of the support of $\nabla^2\phi_\delta(\mathbf{x}_i - \mathbf{x}')$ in (8) is outside the physical flow domain whenever $\mathbf{x}_i$ is near a wall. Unless some special measures are taken to account for this, the amount of vorticity diffusing to points near the

boundary will be distorted. While it is conceivable that ϕ_δ could be modified to have its support entirely within the flow domain, such developments are beyond the scope of the present study. A simpler method, which appears to work satisfactorily for the calculations described below, is to add contributions to (8) from fictitious tiles covering that portion of the support of $\nabla^2\phi_\delta$ extending beyond the solid boundary. These tiles are taken to be reflections through the wall of physical tiles lying near the surface of the flow domain, with vorticity set by extrapolation of the physical vorticity field through the surface. The strength of a tile at $(x_i, -y_i)$ generated by a tile at (x_i, y_i), where $y = 0$ is the boundary, is given by polynomial extrapolation as

$$\begin{aligned}\omega(x_i, -y_i) &= \omega(x_i, 0) + \frac{y_i}{2h}\left(-\frac{3}{2}\omega(x_i, 0) + 2\omega(x_i, 2h) - \frac{1}{2}\omega(x_i, 4h)\right) \\ &\quad + \frac{y_i^2}{4h^2}\left(\frac{1}{2}\omega(x_i, 0) - \omega(x_i, 2h) + \frac{1}{2}\omega(x_i, 4h)\right), \end{aligned} \tag{10}$$

where the vorticities on the right-hand side are computed by an interpolation scheme described below. Some computations were also done using linear extrapolation in place of (10), though these proved to be less accurate. As a result of these considerations, it is now to be understood that the summation in (8) covers the necessary set of reflected tiles, each of which has a strength determined from (10).

Evaluation of (8) is much simplified by introducing an approximation designed to take into account the sheet-like structure of the vortical elements. First, consider the contribution to the vorticity of the ith sheet from a vortex whose streamwise position $x_j \approx x_i$. The approximation can then be made:

$$\begin{aligned}\int_{A_j} \nabla^2\phi_\delta(\mathbf{x}_i - \mathbf{x}')d\mathbf{x}' &= \int_{x_j - l_j}^{x_j + l_j} dx' \int_{y_j - h_j}^{y_j + h_j} dy'\, \nabla^2\phi_\delta(\mathbf{x}_i - \mathbf{x}') \\ &\approx 2h_j \int_{-\infty}^{\infty} dx'\, \nabla^2\phi_\delta(x_i - x', y_i - y_j) \end{aligned} \tag{11}$$

where the integration in x' has been legitimately extended to all of $\Re$, since, according to (9), the integrand contains an exponential term depending on $-(x_i - x')^2$, and so it rapidly approaches zero for $x' \neq x_i$. Substituting for ϕ_δ using (9) and carrying out the integration yields

$$\int_{A_j} \nabla^2\phi_\delta(\mathbf{x}_i - \mathbf{x}')d\mathbf{x}' \approx \frac{h_j}{\sqrt{\pi}\delta^3}\left[e^{-\frac{(y_i - y_j)^2}{\delta^2}} 16\left(\frac{(y_i - y_j)^2}{\delta^2} - \frac{1}{2}\right)\right.$$

$$+\sqrt{2}e^{-\frac{(y_i-y_j)^2}{2\delta^2}}\left(1-\frac{(y_i-y_j)^2}{\delta^2}\right)\Bigg] \tag{12}$$

which is valid when $x_i \approx x_j$. At the opposite extreme, when $\mid x_i - x_j \mid >> 0$, the exponential terms in $\nabla^2\phi_\delta$ force it to be small for all x' in A_j. In this case, the integral of $\nabla^2\phi_\delta(\mathbf{x}_i - \mathbf{x}')$ over A_j is negligble. For the general case where $x_i \neq x_j$, the artifice may be taken of multiplying (12) by a factor $\gamma_{ij} \equiv m((x_i - l_i, x_i + l_i) \cap (x_j - l_j, x_j + l_j))/(2l_i)$ where $m(S)$ is the rectilinear measure of the set S. Thus $\gamma_{ij} = 1$ when $x_i = x_j$ and $l_i = l_j$, and $\gamma_{ij} = 0$ if $(x_i - l_i, x_i + l_i) \cap (x_j - l_j, x_j + l_j) = \emptyset$. The introduction of γ_{ij} follows a procedure adopted in [7] for calculation of the velocity field. Collecting together the previous results, the approximate formula is derived

$$\begin{aligned}\omega_i^{n+1} &= \omega_i^n + \frac{\Delta t}{R}\sum_j \frac{\gamma_{ij}\omega_j^n h_j}{\sqrt{\pi}\delta^3}\left[e^{-\frac{(y_i^n-y_j^n)^2}{\delta^2}}16\left(\frac{(y_i^n-y_j^n)^2}{\delta^2}-\frac{1}{2}\right)\right.\\ &\left.+\sqrt{2}e^{-\frac{(y_i^n-y_j^n)^2}{2\delta^2}}\left(1-\frac{(y_i^n-y_j^n)^2}{\delta^2}\right)\right]\end{aligned} \tag{13}$$

where the sum in (13) is over both the sheets located in the physical domain and the special collection of sheets with strengths given by (10). Since only a relatively small subset of the complete collection of vortical elements intersect $(x_i - l_i, x_i + l_i)$, the complexity of (13) does not make the numerical expense of computing ω_i^{n+1} prohibitive.

Advancement of the vortex elements in time is accomplished by applying (3), (4) and (13) concurrently, so the scheme, as it is implemented here, is fully explicit. This places limits on Δt for stability which may perhaps be avoided by alternative formulations. The applications pursued here, however, are well within the capabilities of the explicit scheme so that the development of other time marching procedures was not pursued further at the present time.

For the purposes of implementing (10), as well as applying boundary conditions and resheeting the flow domain, a scheme is required for computing vorticity at arbitrary points in the flow. Satisfactory performance in this regard was obtained from linear interpolation in the form

$$\omega(\mathbf{x}_i) = \frac{\sum_j \gamma_{ij}\theta_{ij}\omega_j}{\sum_j \gamma_{ij}\theta_{ij}} \tag{14}$$

where $\mathbf{x}_i$ is now meant to denote an arbitrary point in the flow, and $\theta_{ij} \equiv m((y_i - h_i, y_i + h_i) \cap (y_j - h_j, y_j + h_j))/(2h_i)$. The denominator of (14) is necessary to compensate for

overlap of the vortex elements if this should occur. Furthermore, for a boundary layer flow with wall at $y = 0$, each of $y_i - h_i$ and $y_j - h_j$ appearing in the definition of θ_{ij} must be set to zero if they happen to be negative. The sum in (14) is just over the vortices in the immediate neighborhood of a point, so it is of minimal computational cost. When $\mathbf{x}_i$ corresponds to the position of a vortex, then (14) gives the exact result $\omega(\mathbf{x}_i) = \omega_i$.

Some effort was also spent in exploring the possibility that (6) could be made the basis for a non-local vorticity interpolation scheme. By imitating the steps leading to the approximation of $\nabla^2\phi_\delta * \omega$ in (13), the relation

$$\omega(\mathbf{x}_i) \approx \sum_j \frac{\gamma_{ij}\omega_j h_j}{\sqrt{\pi}\delta}\left[4e^{-\frac{(y_i-y_j)^2}{\delta^2}} - \sqrt{2}e^{-\frac{(y_i-y_j)^2}{2\delta^2}}\right] \tag{15}$$

may be derived. Similar to the situation in (13), the sum here must take into account reflected vortices covering that part of the support of ϕ_δ lying in the solid surface. However, for such elements the vorticity is given by (10) which depends on $\omega_i(0)$. As a consequence, to use (15), while at the same time determining $\omega_i(0)$ through imposition of the no-slip condition, requires iteration – a clear disadvantage over (14). Furthermore, test calculations revealed that (15) is subject to substantial errors in the presence of large gradients in the vorticity field. Such conditions occur, for example, in the early time development of the boundary layer forming over an impulsively moved plate. For these reasons (14) provides considerable advantages over (15) in computing ω at arbitrary points in the flow domain.

3. VELOCITY FIELD

In the vortex sheet method as originally developed by Chorin [7], the boundary layer approximation $\omega \approx -\partial u/\partial y$ in integrated form

$$u(x,y) = U(x) + \int_y^{\delta_1(x)} \omega(x,y')dy' \tag{16}$$

provides a basis for the calculation of u. Here, $U(x) = u(x, \delta_1(x))$ and $\delta_1(x)$ is the boundary layer thickness at x. For this study, (16) is evaluated by applying a rectangle rule to the integral giving

$$u(x_i, y_i) = U(x_i) + 2h\sum_{j=1}^{M} \omega(x_i, y_i + 2h(j - 1/2)) \tag{17}$$

where $y_i + 2hM \geq \delta_1(x_i)$, and the vorticities in (17) are computed using (14). A prescription for calculating the wall-normal velocity v has also been given [7] based on the integrated two-dimensional continuity equation:

$$v(x,y) = -\frac{\partial}{\partial x}\int_0^y u(x,y')dy'. \tag{18}$$

It is helpful in evaluating (18) numerically to first rewrite it as

$$v(x,y) = -y\frac{\partial u}{\partial x} - \frac{\partial}{\partial x}\left(\int_0^y y'\omega(x,y')dy'\right) \tag{19}$$

using integration by parts and the relation $\omega = -\partial u/\partial y$. Approximating (19) using central differences for the x derivatives and a rectangle rule for the integral gives

$$\begin{aligned} v(x_i,y_i) &= -y_i\left(\frac{u(x_i+l_i,y_i)-u(x_i-l_i,y_i)}{2l}\right) \\ &\quad -(\Delta y)^2\sum_{j=1}^{M'}(j-.5)\left(\frac{\omega(x_i+l_i,(j-.5)\Delta y)-\omega(x_i-l_i,(j-.5)\Delta y)}{2l}\right) \end{aligned} \tag{20}$$

where $M'\Delta y = y_i$, and Δy is chosen to be as close to $2h$ as possible under the constraint that M' is an integer.

With a view towards the eventual application of this method to three-dimensional turbulent flows, it is of considerable interest to have the capability of computing velocities from vorticities with more generality than (17) and (20). Such a formalism exists in adopting the Biot-Savart integral to the specific properties of sheet-like vortex elements. In three-dimensions this takes the form

$$\mathbf{u}(\mathbf{x},t) = \int_{\Re^3} K(\mathbf{x}-\mathbf{x}')\mathbf{\Omega}(\mathbf{x}',t)d\mathbf{x}' \tag{21}$$

where

$$K(x,y,z) = -\frac{1}{4\pi\mid\mathbf{x}\mid^3}\begin{pmatrix} 0 & -z & y \\ z & 0 & -x \\ -y & x & 0 \end{pmatrix} \tag{22}$$

and $\mathbf{\Omega}$ is the vorticity vector. Following the development in [13,14], the singularity in (21) may be removed by replacing K by $K_\eta = \psi_\eta * K$ where ψ_η is the cutoff function given by

$$\psi_\eta = \begin{cases} 1 & \mid\mathbf{x}\mid\geq\eta \\ \frac{5}{2}\left(\frac{\mathbf{x}}{\eta}\right)^3 - \frac{3}{2}\left(\frac{\mathbf{x}}{\eta}\right)^5 & \mid\mathbf{x}\mid<\eta \end{cases}.$$

In this case

$$K_\eta = \begin{cases} K & |\,\mathbf{x}\,| \geq \eta \\ K\left(\frac{5}{2} - \frac{3}{2}\left(\frac{\mathbf{x}}{\eta}\right)^2\right)\frac{|\mathbf{x}|^3}{\eta^3} & |\,\mathbf{x}\,| < \eta \end{cases}$$

where the cutoff parameter, η, is not necessarily the same as δ appearing in (9). With this modification (21) may be written as

$$\mathbf{u}(\mathbf{x},t) = \sum_j \int_{V_j} K_\eta(\mathbf{x}-\mathbf{x}')\mathbf{\Omega}_j(\mathbf{x}',t)d\mathbf{x}' \tag{23}$$

where V_j is the volume occupied by the jth element. Where appropriate, the summation in (23) may be assumed to include image vortex sheets used to enforce the non-penetration boundary condition.

For two-dimensional flows, $\mathbf{\Omega} = (0,0,\omega)$, and the vortex elements in (23) extend indefinitely in the spanwise direction. Under this circumstance, the z integration over $\Re$ can be carried out explicitly. A closed form solution can also be obtained for the streamwise integration over the limits $x_i - l_i, x_i + l_i$. Finally, the y integral can be modeled by evaluating the integrand at $y' = y_j$. The final result is the non-local relations

$$u(\mathbf{x}_i,t) = \sum_j U_{ij}\omega_j \tag{24}$$

$$v(\mathbf{x}_i,t) = \sum_j V_{ij}\omega_j \tag{25}$$

where U_{ij}, V_{ij} are the respective contributions of the jth vortex sheet to the u and v velocity components at $\mathbf{x}_i$. These are given formally by

$$\begin{aligned} U_{ij} &= -\frac{h_j}{\pi}\left[\tan^{-1}\frac{X_2}{Y} - \tan^{-1}\frac{X_1}{Y} - \left(\tan^{-1}\frac{X_2}{YR_2} - \tan^{-1}\frac{X_1}{YR_1}\right)\right. \\ &\quad + \frac{Y}{2}\left\{\frac{3}{4}\left(\frac{7}{3} - Y^2\right)(X_2R_2 - X_1R_1) + \frac{1}{2}\left(X_2R_2^3 - X_1R_1^3\right)\right. \\ &\quad \left.\left. + \frac{3}{4}\left(Y^4 - \frac{10}{3}Y^2 + 5\right)\left(\tan^{-1}\frac{X_2}{R_2} - \tan^{-1}\frac{X_1}{R_1}\right)\right\}\right] \end{aligned} \tag{26}$$

$$\begin{aligned} V_{ij} &= \frac{h_j}{\pi}\left[\ln\frac{r_2}{r_1} + (R_1 - R_2) + \frac{1}{3}(R_1^3 - R_2^3)\right. \\ &\quad \left. + \frac{1}{5}(R_1^5 - R_2^5) + \ln\frac{1+R_2}{1+R_1} - \frac{1}{2}\ln\frac{1-R_2^2}{1-R_1^2}\right] \end{aligned} \tag{27}$$

where

$$R_m = \begin{cases} \sqrt{1-r_m^2} & r_m < 1 \\ 0 & r_m \geq 1 \end{cases} \qquad m = 1,2$$

$$r_m^2 = X_m^2 + Y^2, \; m = 1, 2,$$

$$X_1 = (x_i - x_j - l_j)/\eta$$

$$X_2 = (x_i - x_j + l_j)/\eta$$

and

$$Y = (y_i - y_j)/\eta.$$

A geometrical interpretation of r_1 and r_2 is given in Fig. 2. Despite the apparent complexity of these formulas, for the great majority of vortex interactions, $r_1, r_2 \geq 1$, in which case (26) and (27) simplify to

$$U_{ij} = -\frac{h_j}{\pi}\left(\tan^{-1}\frac{X_2}{Y} - \tan^{-1}\frac{X_1}{Y}\right) \tag{28}$$

and

$$V_{ij} = \frac{h_j}{\pi}\ln\frac{r_2}{r_1}, \tag{29}$$

respectively. Though it has not been done here, it is likely that a fast vortex method can be developed to improve the efficiency with which (24) and (25) can be applied. This will be the subject of future work.

The relative accuracy of (17) and (24) in computing u, and (20) and (25) in predicting v, may be ascertained by comparing their performances in a zero pressure gradient boundary layer against the exact Blasius velocity field. In this, the initial sheet arrangement in Fig. 1 is used where the exact vorticities are assigned to each vortex element. For this and subsequent discussions of boundary layer flow, lengths are assumed scaled by a streamwise length, L, and velocities by the free stream velocity, U_∞. The Reynolds number $R = U_\infty L/\nu$, and calculations are performed in the non-dimensional flow domain $0 \leq x \leq x^*$, $0 \leq y \leq y^*$, where $x^* = 7.5$ and $y^* = 6.4\sqrt{x^*/R}$. y^* is chosen to be large enough to contain the complete lateral boundary layer growth through position x^*. For the present purposes, $R = 1000$, $N = 1200$ (i.e. a 60×20 arrangement), $l = .05$, and $h = .0138$. Here and in the following, $\eta = C_\eta\sqrt{h}$ with $C_\eta = .5$. Figures 3a and 3b show the u predictions on the lines $y = .1$ and $x = 2.5$, respectively, while Figs. 4a and 4b contain similar plots of the v velocity.

It is clear from Fig. 3a that (17) captures the streamwise velocity with high accuracy along the entire length of the boundary layer, including both the leading edge and the

exit plane. In contrast, (24) is reasonably accurate only until $x \approx 4$, after which it diverges from the Blasius solution, finally becoming entirely unphysical at $x \approx 7$ where it sharply rises. The poor performance of (24) reflects the absence of contributions from vorticity lying beyond x^*, a flaw which cannot be simply corrected in a boundary layer calculation, since this vorticity can only be obtained with knowledge of the velocity in the same region, which itself requires the vorticity further downstream and so on. Figure 3a also shows that (24) is somewhat inaccurate at the leading edge of the boundary layer. This may be attributed to the failure of the Blasius solution to accurately account for the vorticity field at and around the upstream end of the flat plate. For example, the Blasius similarity solution predicts that v and ω are singular at $x = 0$.

The accuracy of (17) also holds up in the cross stream direction as shown in Fig. 3b, while (24) shows small deviations from the exact velocity near the wall and outer edge of the boundary layer. In the former case, these may be due to the radial symmetry of ψ_η. It is evident from these considerations that (17) is to be preferred over (24) in the calculation of boundary layer flows, and so it is used exclusively in what follows. In more general situations, where the use of (17) may be impractical, the methodology embodied in (24) may find application.

In the case of the wall-normal velocity, Figs. 4a and 4b show that each of the formulas (20) and (25) are potentially useful, but neither is free of problems. As in the case of (24), (25) suffers from the finite extent of the calculation domain by diverging from the correct solution, though in this instance, it remains accurate to at least $x \approx 6$. Near the leading edge it deviates from the unphysical singularity of the Blasius solution. According to Fig. 4b, (25) is fairly accurate across the boundary layer, though it underpredicts v near the outer edge and slightly overpredicts it at the wall. These errors are likely due to the long range effect of the missing downstream vorticity, the form of ψ_η, and the tile resolution in the wall-normal direction. Note that the non-penetration boundary condition is identically satisfied here with the use of image vortex sheets.

Equation (20) also displays some undesirable properties in its representation of v, though the overall trend is captured. Particularly evident in Figs. 4a and b is its susceptability to streamwise oscillations which are quite noticeable near the leading edge. The relative amplitude of these fluctuations is small in comparison to the streamwise

velocity so that their effect in calculations is minimal. It should be remarked that for sufficiently coarse streamwise resolution, v associated with (25) is also subject to significant oscillations. In this case there is a minimum density of elements in the streamwise direction necessary for (25) to yield a smooth prediction of v such as is displayed in Fig. 4b. It is clear that between the two approaches, only (20) is useful near the exit region. Consequently, either (20) can be used throughout the boundary layer, or a hybrid scheme can be employed wherein (20) is used near the downstream end and (25) is used near the leading edge and as far downstream as it remains accurate. Calculations of the Blasius boundary layer performed below use such a hybrid approach while the Falkner-Skan flow is treated using (20) exclusively. In the latter case, the vorticity field is not subject to large gradients at the leading edge as appear in Blasius flow. In addition, test computations showed that a relatively high streamwise density of sheets is needed to force a smooth response from (25) in this instance, so there is little incentive for applying (20) to this case. In summary, it appears that there are advantages to using either or both of (20) and (25) depending on the particular flow under consideration.

4. BOUNDARY CONDITIONS

The no slip condition is satisfied locally by assigning vorticity to the row of half thickness sheets kept fixed along the solid wall. This is done after the computation of $\mathbf{x}^{n+1}$ and ω^{n+1} from (3), (4) and (13), via the first order formula

$$\omega(x_i, 0) = -\frac{u(x_i, h)}{h} \tag{30}$$

where $u(x_i, h)$ is computed from (17). Though (30) appears to be adequate for the present purposes, it is likely that greater accuracy may be attainable with higher order formulations. The potential advantages of such modifications will be considered in future studies.

Unlike the random vortex method, deterministic approaches require vortex elements – even possibly of zero vorticity – to be present at all points of the flow that may be the recipient of vorticity from viscous transfer. As a result, special care must be taken, particularly at boundaries, to insure that artificial voids in the element population are

not created which would distort the diffusion process. For the present applications this chiefly means making special provision for the influx of vorticity-free fluid at the upstream boundary and allowing for the drift of fluid away from the solid boundary. In each of these cases the integrity of the vortex sheet calculation can be maintained by permitting special groups of vortex elements to deform according to the local flow conditions.

At an inflow boundary, such as $x = 0$ in Fig. 1, the movement of new fluid into the computational domain can be accounted for by allowing the column of sheets with ends at $x = 0$ to elongate from one time step to the next. This may be conceptualized as a two step process in which the sheets first convect with the flow, and then the vorticity-free fluid which has entered the flow domain behind them is appended to their upstream ends. This procedure assures that the tiles are always maintained with large aspect ratios so that the validity of the approximations in (13) and (25) remain valid. When one of the sheets reaches a length $> 4l$, a sheet of length $2l$ is subtracted from it at its downstream end – which is then treated like the other elements – while the remaining part of the original sheet becomes a new boundary element that now assumes the role of lengthening to eventually divide again in the future. Since the growth of the boundary sheets is due to the infusion of zero vorticity fluid, it is necessary to reduce their vorticity accordingly at each time step. This is formally accomplished by multiplying the newly computed vorticity ω_i^{n+1} from (13), by the factor x_i^n/x_i^{n+1} which effectively averages ω_i between the zero vorticity fluid entering the flow domain and that previously existing in the vortex element.

It is in the nature of the Blasius boundary layer flow for fluid particles to slow and convect away from the surface as they pass over it. This tendency, if left unchecked, creates holes in the vortex element representation near the solid boundary. To counteract this, each of the elements in the second horizontal row of Fig. 1, i.e. adjacent to the wall elements, are allowed to increase in thickness by a process similar to the lengthening which was done for the vortices on the upstream boundary. In this, a sheet is first convected with the flow to position (x_i^{n+1}, y_i^{n+1}) after which the fluid in the gap region between it and the closest wall vortices is appended to it thereby increasing its thickness. As before, the vorticity of the element is then adjusted to reflect the addition of new

fluid. In this instance, after ω_i^{n+1} is computed from (13), it is corrected by the formula

$$\omega_i^{n+1} = \frac{\omega_i^{n+1} 2h_i^n + \omega(x_i^n, h)(y_i^{n+1} - h_i - h)}{2h_i^n + (y_i^{n+1} - h_i - h)}. \tag{31}$$

which represents a weighted average of ω_i^{n+1} and $\omega(x_i^n, h)$ – where the latter quantity is the vorticity along the lower boundary of the element before its convection. Note that $y_i^{n+1} - h_i - h$ is the gap thickness, and the denominator in (31) is the new thickness of the vortex sheet.

The vortices in the second row cannot be allowed to grow indefinitely, since they would then eventually have a small aspect ratio. At the same time, it is not feasible to periodically halve them, such as is done along the leading edge, since they do not grow in length along the principal flow direction, i.e., newly divided vortices would have a high likelihood of overlapping downstream vortices. Consequently, the only acceptable means of maintaining the vortex sheet calculation is to periodically regrid the sheets in order to insure the continual presence of a regular arrangement of vortices filling all of the flow domain. Resheeting is done by recreating the arrangement of tiles in Fig. 1 with vorticities determined from (14).

At the downstream boundary, all tiles for which $x_i - l_i > x^*$ are eliminated from the calculation so that the total number of sheets stays approximately constant in time. Since the computation of u, v, ω and $\nabla^2\omega$ at locations $x > x^* - l$ via (13), (14), (17), (20) and (25) depends on having elements for which $x_i - l_i > x^*$, special measures must be taken to prevent errors in computing flow properties at these positions. In the following, this problem is avoided by using linear extrapolation at points $x > x^* - l$. For example, u is computed from

$$u(x, y) = u(x^* - l, y) + \left(\frac{u(x^* - l, y) - u(x^* - 3l, y)}{2l}\right)(x - x^* - l) \tag{32}$$

and similarly for v, ω and $\nabla^2\omega$. Use of (32) or equivalent appears to be necessary, e.g., numerical tests showed that zero streamwise gradient conditions for $x > x^* - l$ had the effect of impairing the proper boundary layer growth well upstream of x^*.

5. COMPUTED RESULTS

Before considering the calculation of boundary layers, a useful test of the algorithm in a simpler setting is its application to the non-steady channel flow developing from a state of rest after the sudden imposition of a presure gradient. For a non-dimensionalization based on the channel half-width and average mass flow velocity, u_m, the exact steady state solution in this case is $\omega(y) = -3(1-2y)$. For this one-dimensional flow, the vortex sheets may be taken to be infinitely long in the streamwise direction with concomitant simplification of (13), (14) and (17). The wall-normal velocity is zero, as well, and may be eliminated from consideration. To apply (17) while maintaining time accuracy, it is necessary to have available the correct centerline velocity at all times. This may be obtained indirectly through knowledge of u_m which can be determined from a discretization of the exact relation

$$\frac{du_m}{dt} = \frac{1}{R}(3 + \omega(0,t)). \tag{33}$$

In particular, applying a first order approximation to (33), $u_m(t+\Delta t)$ can be determined from $u_m(t)$ and $\omega(0,t)$. The correct centerline velocity at time $t+\Delta t$ is that which insures that the computed mass average velocity is equal to $u_m(t+\Delta t)$.

Calculations were performed with $R = 1000$, $h = .02$ and $\delta = C_\delta\sqrt{h}$ where $C_\delta = .2$. It is evident from Fig. 5 that the method predicts the asymptotic vorticity field with very high accuracy. Of perhaps more significance is the degree to which the approach to the equilibrium state is computed accurately. An indication of this is shown in Fig. 6 comparing the exact time history of u at the point $y = .2$ in the channel with that from the present algorithm. The agreement is quite good. Furthermore, Fig. 7 illustrates, through a comparison of the exact and predicted vorticities across the half channel at the intermediate time $t = 100$, that time accuracy is maintained at all points in the channel during the computation. Similar calculations to these were also made assuming impulsive motion of the fluid in the channel, that is, initial condition $u = 1$. In this case, the predicted transient did show some discrepancies from the exact solution due to inaccuracies in resolving the initial vorticity discontinuity.

Computations of the Blasius and Falkner-Skan boundary layers were performed by impulsively moving the fluid in an initially zero vorticity field and then computing until

the solution converged to a steady state condition. The Blasius boundary layer was calculated at $R = 10,000$ using a variety of grid sizes and values of the parameters δ and η. The performance of the algorithm in this flow is summarized in Figs. 8 - 10 comparing the exact similarity solution to numerical calculations using 1200 elements in a 60×20 initial arrangement so that $l/h = 14.3$ and 2700 elements in a 90×30 grid with the same aspect ratio. As before, $\delta = .5\sqrt{h}$, $\eta = .2\sqrt{h}$ and the computed solution was essentially independent of these parameters over a significant range.

The streamwise velocity on a wall-normal cut through the boundary layer at $x = 2.5$ is shown in Fig. 8a. The solutions agree well with the Blasius profile, with the better resolved one somewhat more accurate. The situation is similar in Fig. 8b showing u along a streamwise cut on the line $y = .05$. Here, the improved resolution in the x direction results in a noticeable gain in accuracy. Equivalent plots of the wall-normal velocities are shown in Figs. 9a and b. Clearly, the predictions of v are credible, though the relative errors are somewhat greater than in the case of u. Since the magnitude of v is much smaller than u, however, the error in absolute terms is actually much lower here than for the streamwise velocity. Figure 9b is particularly instructive since it reveals the effect of streamwise resolution on the appearance of fluctuations in the velocity field. These are significant near the leading edge and may be attributed to the large vorticity gradients in this region that are difficult to accommodate with a coarse covering of vortex tiles. Evidently, an increase from 60 to 90 tiles in the x direction effectively removes these fluctuations. As in the case of Fig. 4a, Fig. 9b shows that the numerical solution does not mimic the singularity in the Blasius solution.

Predictions of the vorticity are shown in Fig. 10. On the line $x = 2.5$ in Fig. 10a, ω is closely predicted except at the wall, where it tends to be too large in magnitude. This error is much reduced by increasing the resolution. Figure 10b, containing a plot of the vorticity on the wall surface, shows the large variation in ω near the leading edge of the flat plate at this Reynolds number. With refined resolution, the prediction of wall vorticity is substantially improved, and with it, presumably, the overall downstream predictions of u and v as observed above in Figs. 8b and 9b.

The capabilities of the present scheme in describing the boundary layer forming downstream of a stagnation point are illustrated in Figs. 11 - 13 covering u, v and ω. In this

case, results are presented for a calculation with $N = 2250$ elements in a 75×30 arrangement. Excellent agreement with the similarity solution for u is found along x and y cuts as shown in Fig. 11. In particular, u is free of the unphysical near wall behavior which is evident in calculations of this flow using the random sheet method [25]. Similarly, good predictions are found in regards to v as displayed in Fig. 12. The small error visible in Fig. 12b reflects the degree of wall-normal resolution. Figure 13 shows generally good predictions of the vorticity field, though there is a systematic loss of accuracy in the wall vorticity prediction with downstream distance. Since the boundary layer thickness is independent of x for this flow, and the wall vorticity increases linearly with downstream distance, as seen in Fig. 13b, it is clear that the spanwise resolution of the sheet calculation is systematically deteriorating in the streamwise direction. This may account for the loss of accuracy. Greater resolution of sheets should help considerably in counteracting this trend.

Some attention was paid to exploring the effect of the time interval between resheetings, say t_{rs}, on the computed solutions. Generally, the calculations showed that as long as t_{rs} was not too large, the converged solutions were independent of the resheeting process. A useful means of investigating the influence of t_{rs} is through observing time traces of the computed vorticity field at a fixed point for different values of t_{rs}. The results of such a comparison are shown in Fig. 14 for the point $x = 2.5, y = .025$ in the Blasius boundary layer simulation at $R = 10000$ with $N = 1200$. The cases $t_{rs} = .025, .25, .5$ and 1.0 are considered, where $\Delta t = .025$ and $t_{rs} = .25$ was used in the previously discussed Blasius boundary layer calculations.

At the largest value, $t_{rs} = 1$, ω has substantial oscillations. Beyond $t = 8$ in Fig. 14 these have a primary period of one which is clearly tied to the resheeting process. Higher frequency disturbances are also visible in this curve, which originate from other aspects of the numerical algorithm. For example, as many as 8 vortex subdivisions would have occurred from vortices on the front boundary during a unit time interval. While the calculation with $t_{rs} = 1$ appears to be stable, its accuracy is unacceptable. For larger values of t_{rs} the solution will ultimately become unstable, with the appearance of a disorderly geometrical arrangement of sheets. As t_{rs} decreases below 1, Fig. 14 shows that the oscillations reduce in amplitude and then vanish entirely. For $t_{rs} = .5$, the

fluctuation magnitude is much less than at $t_{rs} = 1$ and the frequency of the disturbance is closely tied to the resheeting. For $t_{rs} \leq .25$ the oscillations are no longer visible. Below the oscillatory range of t_{rs}, resheeting has a very small effect on the equilibrium solution reached in the calculation. This and other effects of t_{rs} would most likely be reduced by enhancing the accuracy of the interpolation scheme (14) and other facets of the method. Selection of t_{rs} in applications should be guided by considerations of accuracy and stability, since the computational time needed in regridding using (14) is only a small part of the total iteration time. At the same time, to the extent that resheeting is a smoothing process, it is not desirable to continuously resheet, e.g. at every time step. Evidently, t_{rs} should be taken as large as possible but below the onset of oscillations.

The instantaneous realizations of boundary layer flow produced by the present algorithm match the exact similarity solutions without the spatial velocity fluctuations normally associated with the random vortex method. This attribute of the approach may be quantized by the observation that the root-mean-square velocity fluctuation magnitude, $u' \equiv (\overline{(u - \overline{u})^2})^{1/2} << 1$, where the overbar denotes time averaging. It is instructive to contrast this with u' derived from an equivalent calculation of the Blasius boundary layer using the random sheet method. This is plotted in Fig. 15 with an equivalent plot for v' in Fig. 16. For comparison, the values of u' and v' computed in a turbulent boundary layer simulation by Spalart [24] are also shown. To make the comparisons meaningful, u' and v' are given in wall variables, i.e. scaled by the friction velocity $u_\tau \equiv \sqrt{\nu \partial u / \partial y(0)}$ and the abscissa here is $y' = y/\delta_1$. These plots show that the pseudo turbulent energy in the random vortex method dwarfs the real energy in a true turbulent flow. In the case of v' the artificial noise is undiminished at the outer edge of the boundary layer due to the peculiarities of formula (20), which is used in the random sheet method. An example of the phenomenon displayed in Figs. 15 and 16 may be found in the back step flow calculations reported by Gagnon, et al. [15] where the turbulent stresses are significantly overpredicted adjacent to the boundaries. Evidently, it is not reasonable to pretend that the chaotic velocity field associated with the two-dimensional random vortex method is a substitute for the real three-dimensional turbulent flow.

6. CONCLUSIONS

The deterministic approach for computing vorticity diffusion developed by Fishelov [13] has been shown to be adaptable to the construction of a vortex sheet method for flows containing solid boundaries. Numerical predictions of channel and boundary layer flows suggest that the approach can be successfully applied to a range of useful applications. The outlook is good that after suitable generalization to take into account spanwise velocities, the method can provide a reliable means of accounting for viscous diffusion in turbulent flow simulations. In particular, it is envisioned that the present technique could be employed in conjunction with a method for simulating the dynamics of three-dimensional vortical structures.

A number of directions to take in improving the approach are worthy of consideration in future work. In particular, the computational efficiency of the algorithm can be enhanced in several ways including developing fast multipole formulas for Eqs. (24) and (25). Various aspects of the algorithm, including the treatment of the special sets of deforming vortices near the boundaries, the interpolation scheme (14), the resheeting process, the extrapolation condition (10) and the time differencing, may be recast in higher order form to improve accuracy beyond that achieved here.

ACKNOWLEDGEMENT

This research was supported in part by ONR Grant N00014-93-10184 and in part by the Applied Mathematical Sciences Subprogram of the Office of Energy Research, U. S. Department of Energy under Contract DE-AC03-76SF00098 while the author was a visiting professor at the Department of Mathematics, University of California, Berkeley, and at Lawrence Berkeley Laboratory.

REFERENCES

1. C. R. Anderson, A method of local corrections for computing the velocity field due to a distribution of vortex blobs, *J. Comput. Phys.* **61**, 111 (1985).

2. S. B. Baden and E. G. Puckett, A fast vortex method for computing 2D viscous flow, *J. Comput. Phys.* **91**, 278 (1990).

3. T. Beale and A. Majda, High order accurate vortex methods with explicit velocity kernels, *J. Comput. Phys.* **58**, 188 (1985).

4. P. S. Bernard, J. M. Thomas and R. A. Handler, Vortex dynamics and the production of Reynolds stress, *J. Fluid Mech.* **253**, 385 (1993).

5. A. Cheer, A study of incompressible 2-D vortex flow past a circular cylinder, *SIAM J. Sci. Stat. Comput.*, **4**, 685 (1983).

6. A. Cheer, Unsteady separated wake behind an impulsively started cylinder, *J. Fluid Mech.* **201**, 485 (1989).

7. A. J. Chorin, Vortex sheet approximation of boundary layers, *J. Comput. Phys.* **27**, 428 (1978).

8. A. J. Chorin, Hairpin Removal in Vortex Interactions II, Lawrence Berkeley Laboratory Report LBL-30927 (1991).

9. A. J. Chorin, *Vorticity and Turbulence* (Springer-Verlag, New York, 1994).

10. G. H. Cottet, A particle-grid superposition method for the Navier-Stokes equations, *J. Comput. Phys.* **89**, 301 (1990).

11. G. H. Cottet and S. Mas-Gallic, A particle method to solve the Navier-Stokes system, *Numer. Math.* **57**, 805 (1990).

12. P. Degond and S. Mas-Gallic, The weighted particle method for convection-diffusion equations, Part I: The case of an isotropic viscosity, Part II: the anisotropic case, *Numer. Math.* **53**, 485 (1989).

13. D. Fishelov, A new vortex scheme for viscous flows, *J. Comput. Phys.* **86**, 211 (1990).

14. D. Fishelov, Vortex methods for slightly viscous three-dimensional flow, *SIAM J. Sci. Stat. Comput.* **11**, 399 (1990).

15. Y. Gagnon, A. Giovannini and P. Hebrard, Numerical simulation and physical analysis of high Reynolds number recirculating flows behind sudden expansions, *Phys. Fluids A* **5**, 2377 (1993).

16. L. Greengard, The numerical solution of the N-Body problem, *Computers in Physics*, Mar/Apr, 142 (1990).

17. L. Greengard and V. Rokhlin, A fast algorithm for particle simulations, *J. Comput. Phys.* **73**, 325 (1987).

18. W. D. Henshaw, H.-O. Kreiss and L. G. Reyna, On smallest scale estimates and a comparison of the vortex method to the pseudo-spectral method, *Vortex Dynamics and Vortex Methods, Lectures in Applied Mathematics Vol. 28*, edited by C. R. Anderson and C. Greengard (American Mathematical Society, Providence, 1991), p. 303.

19. P. D. Koumoutsakos, Direct numerical simulations of unsteady separated flows using vortex methods, Ph.D. thesis, Caltech (1993).

20. E. G. Puckett, Vortex methods: an introduction and survey of selected research topics, in *Incompressible computational fluid dynamics: trends and advances*, edited by M. D. Gunzburger and R. A. Nicolaides (Cambridge University Press, Cambridge, 1993), p. 335.

21. G. Russo, A deterministic vortex method for the Navier-Stokes equations, *J. Comput. Phys.* **108**, 84 (1993).

22. H. Schlichting, *Boundary Layer Theory, 7th Ed.*, (McGraw-Hill, New York, 1979).

23. J. A. Sethian, J.-P. Brunet, A. Greenberg and J. P. Mesirov, Vortex methods and massively parallel processors, *Vortex Dynamics and Vortex Methods, Lectures in Applied Mathematics Vol. 28*, edited by C. R. Anderson and C. Greengard (American Mathematical Society, Providence, 1991), p. 597.

24. P. R. Spalart, Direct simulation of a turbulent boundary layer up to $R_\theta = 1410$, *J. Fluid Mech.* **187**, 61, (1988).

25. D. M. Summers, A random vortex simulation of Falkner-Skan boundary layer flow, *J. Comput. Phys.* **85**, 86 (1989).

26. F. S. Winckelmans and A. Leonard, Contributions to vortex particle methods for the computation of three-dimensional incompressible unsteady flows, *J. Comput. Phys.* **109**, 247 (1993).

FIGURE CAPTIONS

Fig. 1. Initial configuration of sheets for boundary layer calculations.

Fig. 2. Geometry of sheet interactions.

Fig. 3. Tests of u predictions: ——, Eq. (17); - - - -, Eq. (24); and ∘, Blasius solution. (a) $y = .1$, (b) $x = 2.5$

Fig. 4. Tests of v predictions: ——, Eq. (20); - - - -, Eq. (25); and ∘, Blasius solution. (a) $y = .1$, (b) $x = 2.5$

Fig. 5. Steady state vorticity field in channel flow: ——, computed; ∘, exact solution.

Fig. 6. Time history of u at $y = .2$ in channel flow: ——, computed; ∘, exact solution.

Fig. 7. Vorticity field in channel flow at $t = 100$: ——, computed; ∘, exact solution.

Fig. 8. Comparisons of u predictions in Blasius boundary layer: - - - -, $N = 1200$; ——, $N = 2700$; and ∘, Blasius solution. (a) $x = 2.5$, (b) $y = .05$.

Fig. 9. Comparisons of v predictions in Blasius boundary layer: - - - -, $N = 1200$; ——, $N = 2700$; and ∘, Blasius solution. (a) $x = 2.5$, (b) $y = .05$.

Fig. 10. Comparisons of ω predictions in Blasius boundary layer: - - - -, $N = 1200$; ——, $N = 2700$; and ∘, Blasius solution. (a) $x = 2.5$, (b) $y = 0$.

Fig. 11. Comparisons of u predictions in stagnation flow boundary layer: ——, computed; and ∘, Falkner-Skan solution. (a) $x = 2.5$, (b) $y = .1$.

Fig. 12. Comparisons of v predictions in stagnation flow boundary layer: ——, computed; and ∘, Falkner-Skan solution. (a) $x = 2.5$, (b) $y = .1$.

Fig. 13. Comparisons of ω predictions in stagnation flow boundary layer: ——, computed; and ∘, Falkner-Skan solution. (a) $x = 2.5$, (b) $y = 0$.

Fig. 14. Effect of t_{rs} on time record of ω at $x = 2.5, y = .025$ in a Blasius boundary layer. - - - -, $t_{rs} = .025$; - · -, $t_{rs} = .25$; · · ·, $t_{rs} = .50$; ——, $t_{rs} = 1$.

Fig. 15. u'/u_τ. ——, random sheet method; ∘, turbulent boundary layer in reference [24].

Fig. 16. v'/u_τ. ——, random sheet method; ∘, turbulent boundary layer in reference [24].

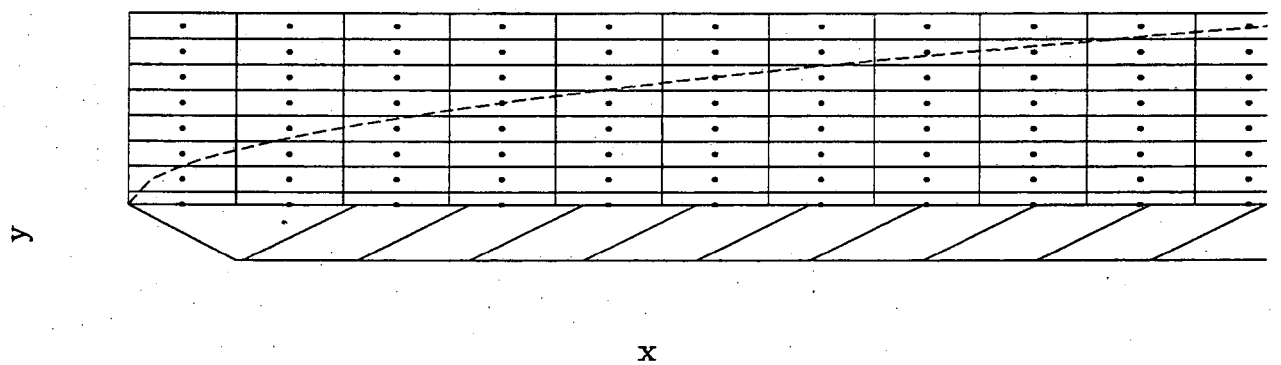

Fig. 1. Initial configuration of sheets for boundary layer calculations.

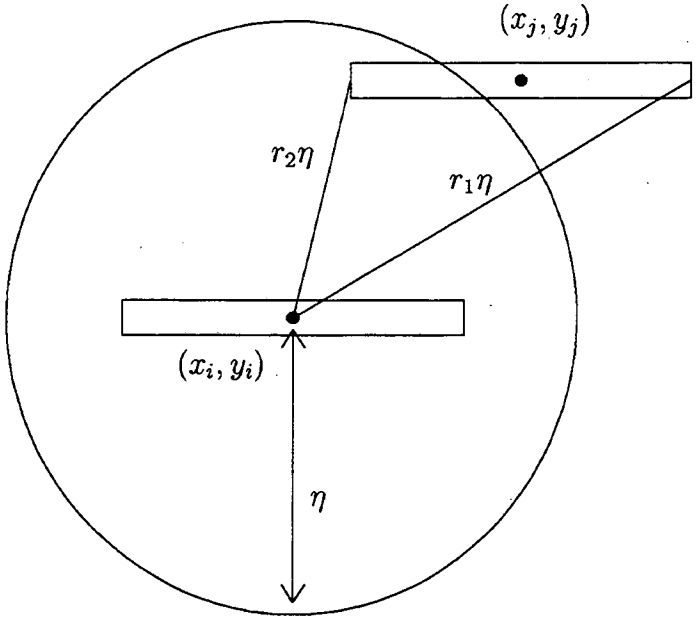

Fig. 2. Geometry of sheet interactions.

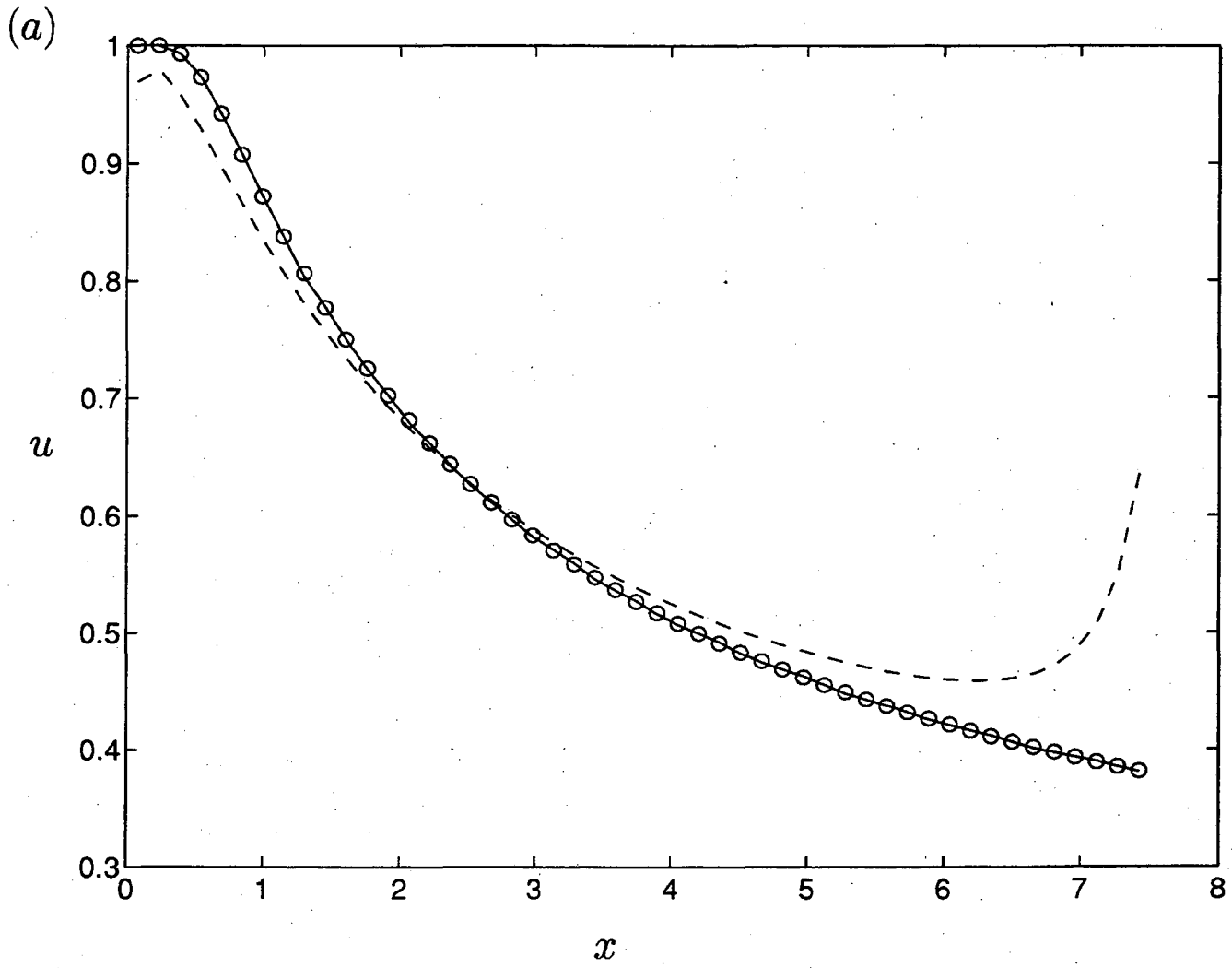

Fig. 3. Tests of u predictions: ——, Eq. (17); - - - -, Eq. (24); and ∘, Blasius solution. (a) $y = .1$, (b) $x = 2.5$

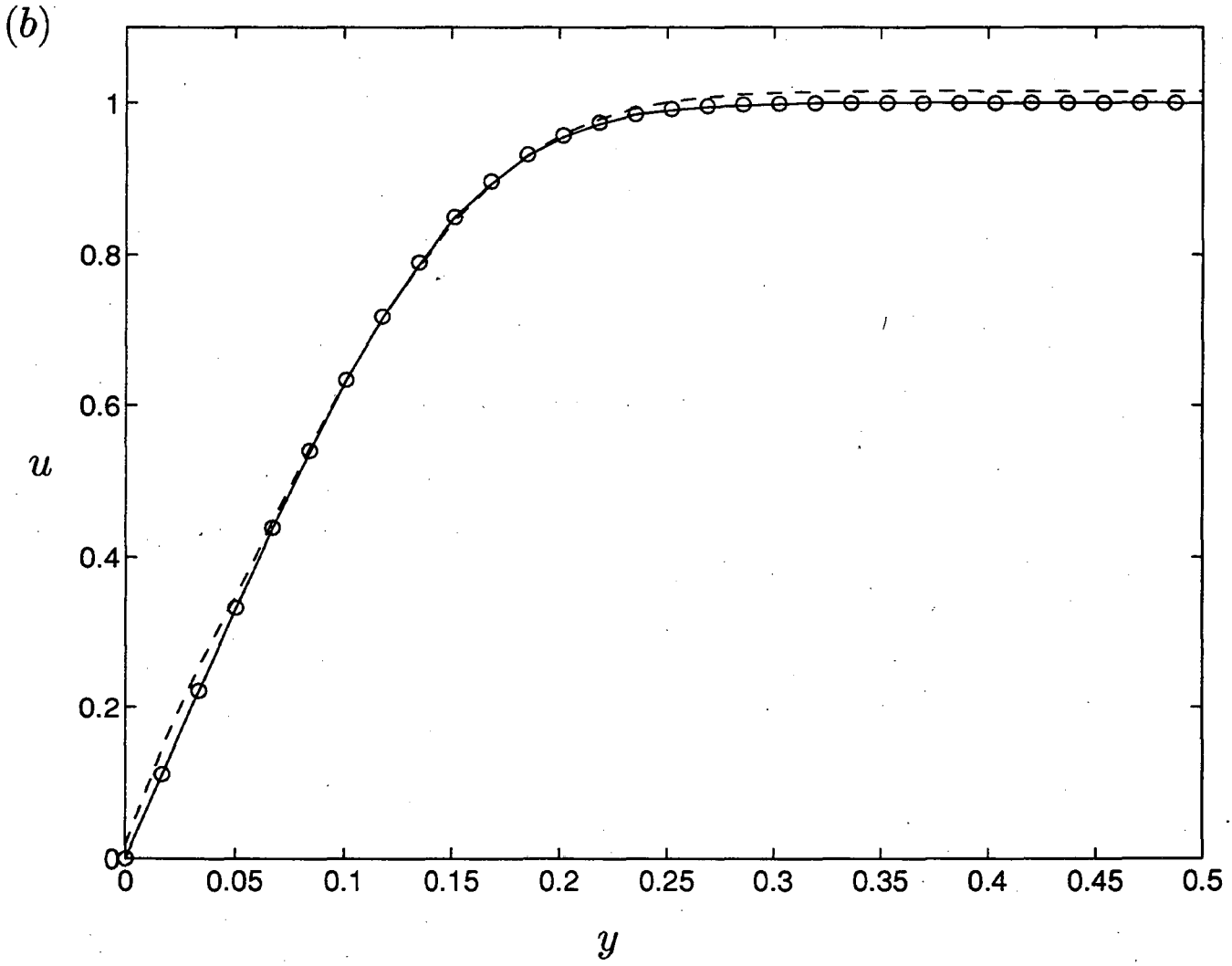

Fig. 3. Tests of u predictions: ——, Eq. (17); - - - -, Eq. (24); and ∘, Blasius solution. (a) $y = .1$, (b) $x = 2.5$

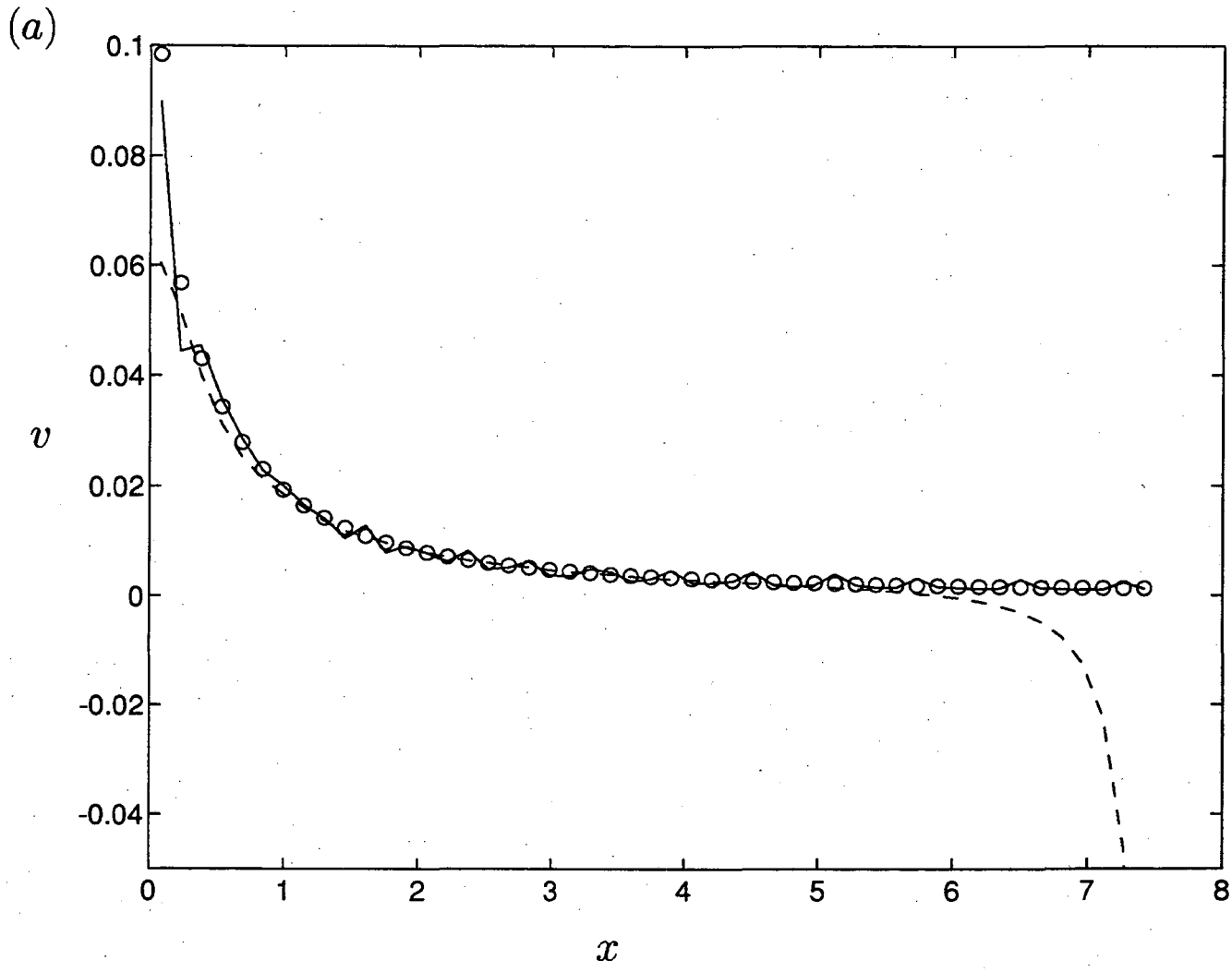

Fig. 4: Tests of v predictions: ——, Eq. (20); - - - -, Eq. (25); and ∘, Blasius solution. (a) $y = .1$, (b) $x = 2.5$

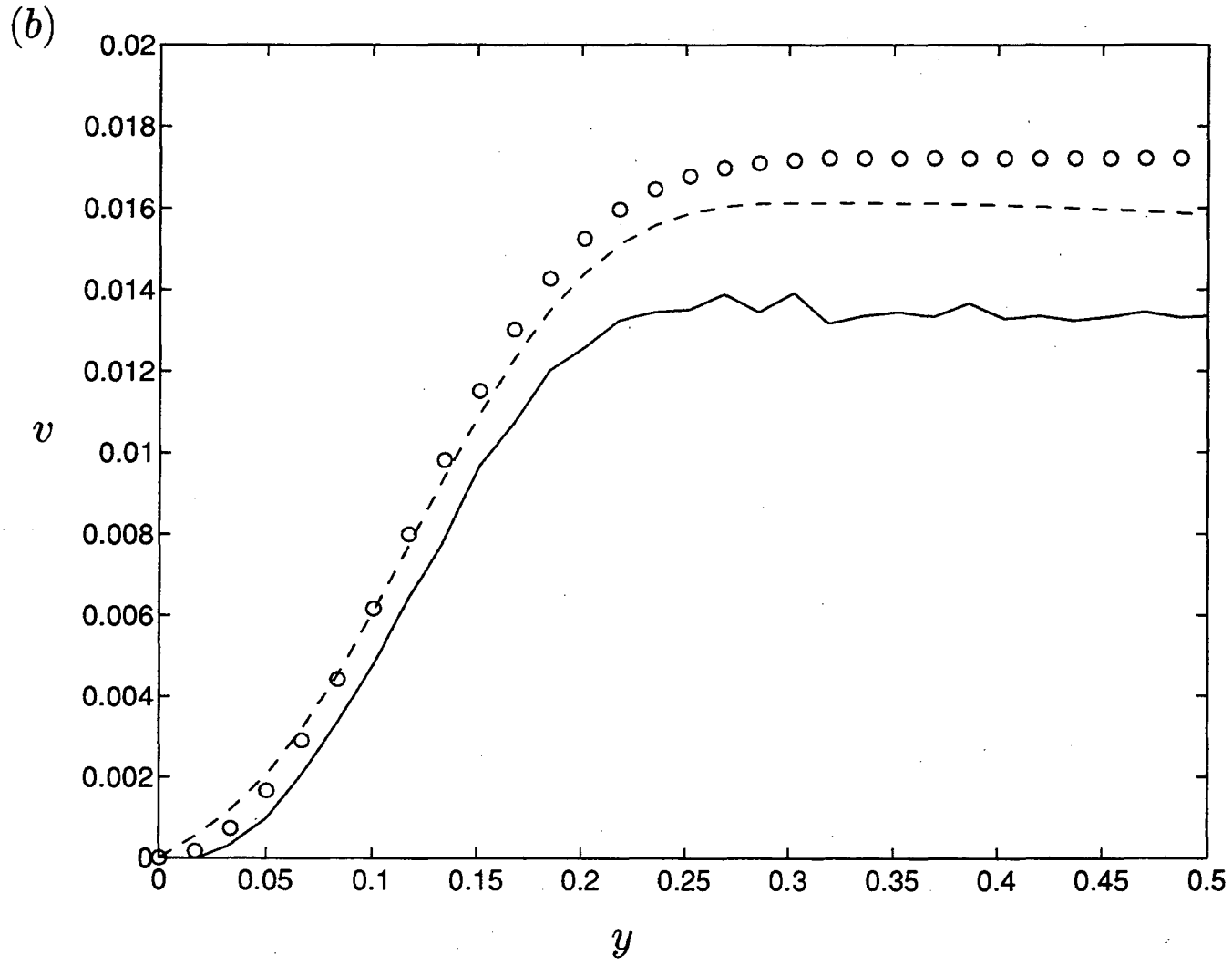

Fig. 4. Tests of v predictions: ——, Eq. (20); - - - -, Eq. (25); and ∘, Blasius solution. (a) $y = .1$, (b) $x = 2.5$

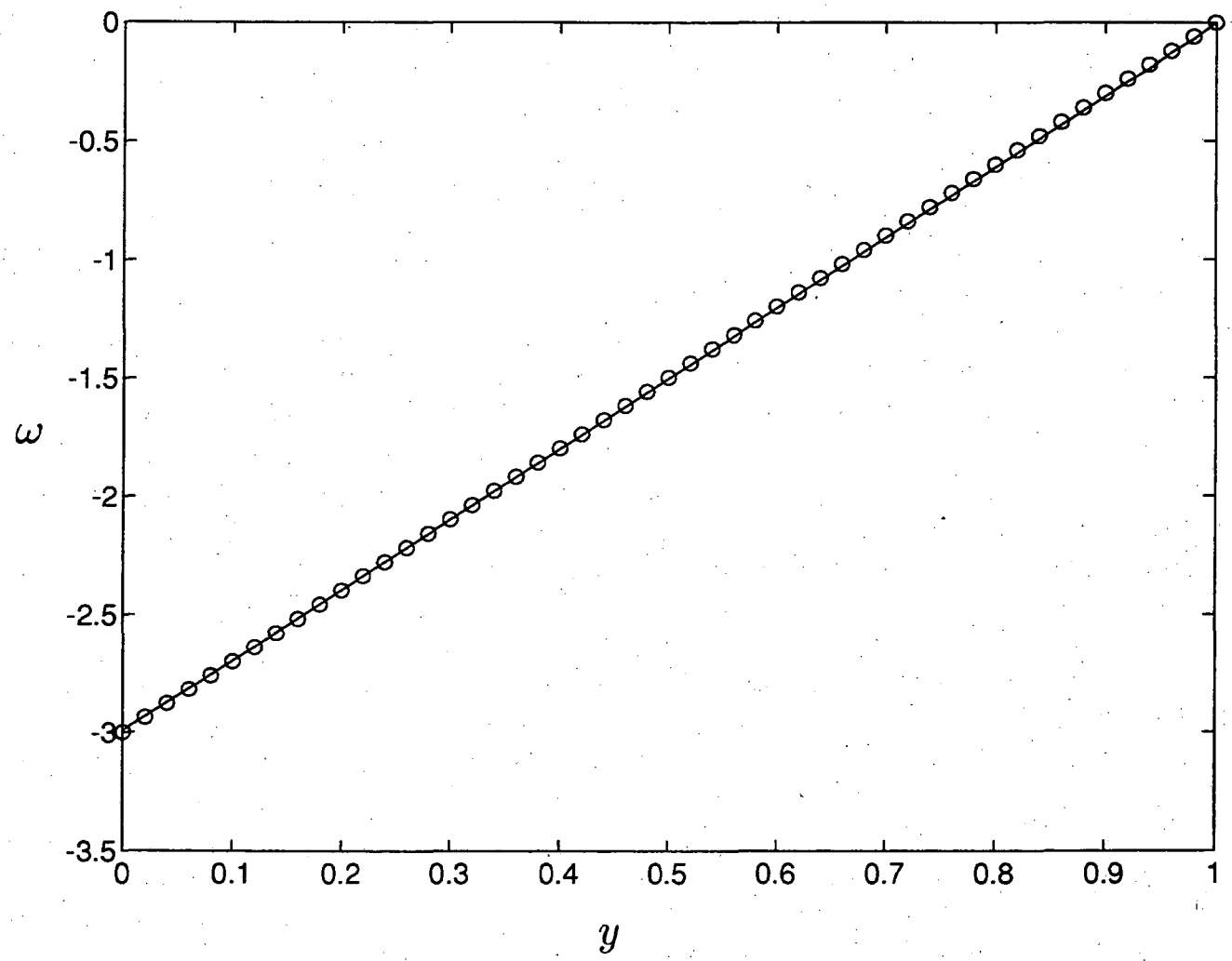

Fig. 5. Steady state vorticity field in channel flow: ——, computed; ∘, exact solution.

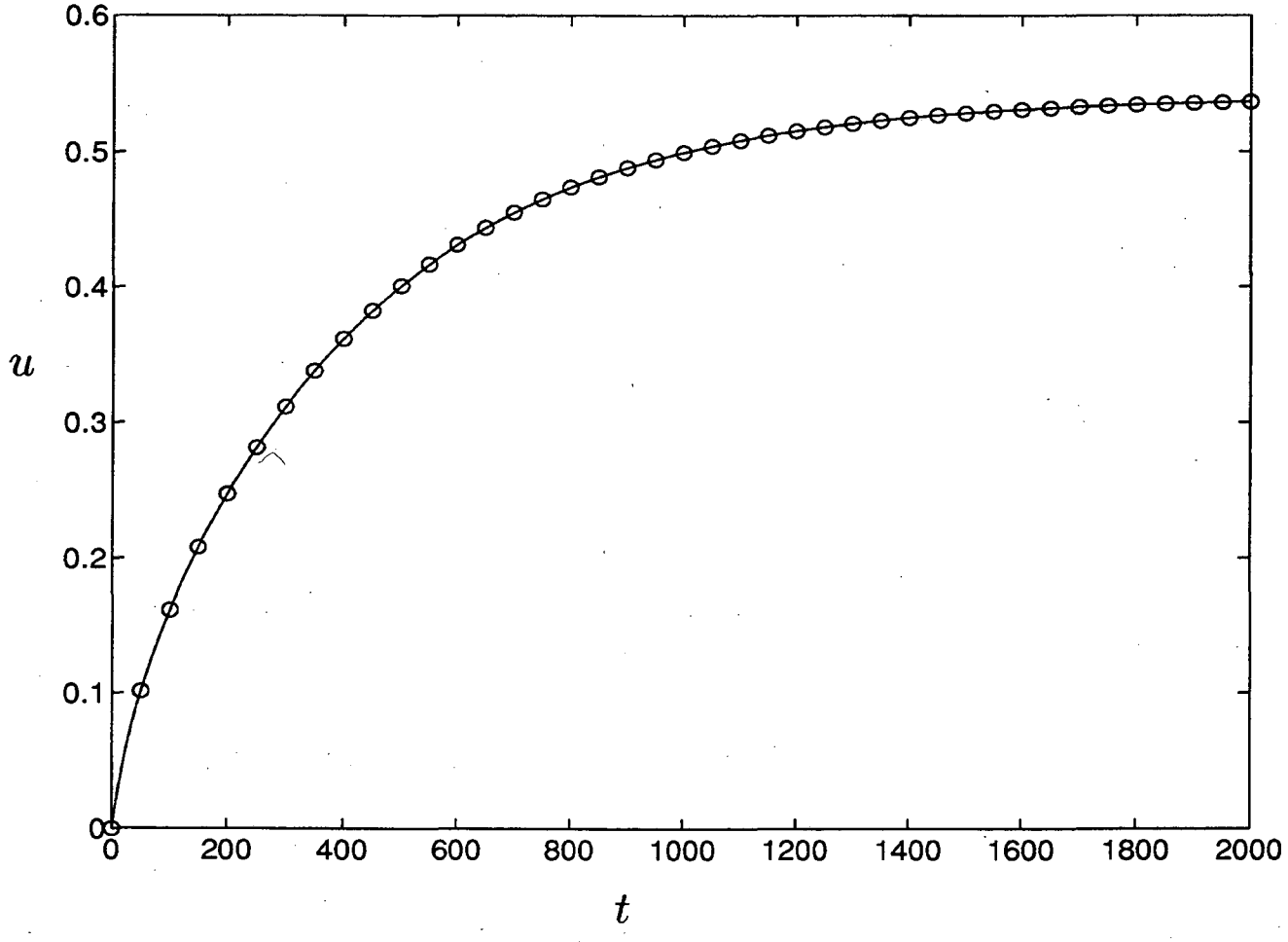

Fig. 6. Time history of u at $y = .2$ in channel flow: ——, computed; ∘, exact solution.

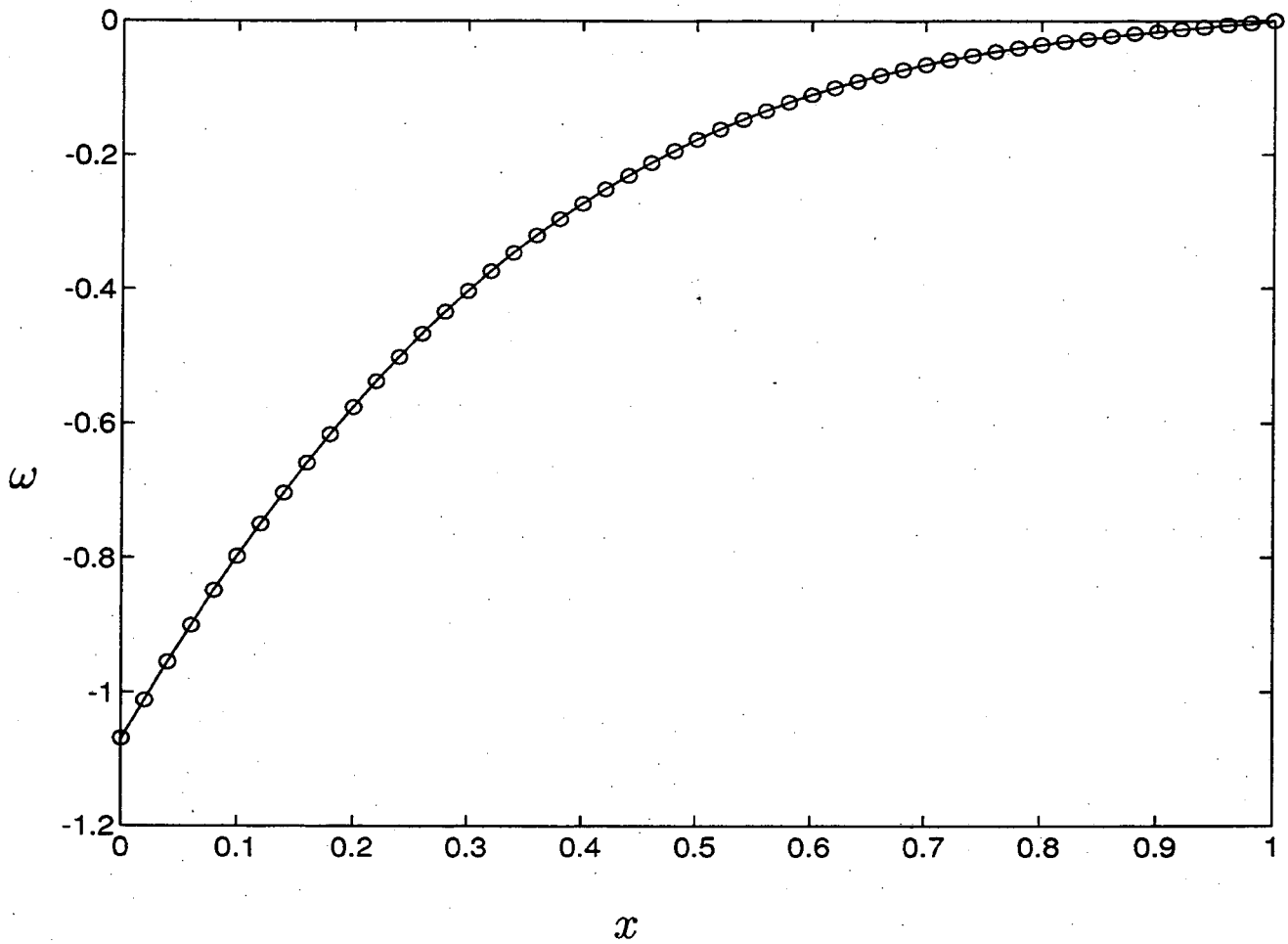

Fig. 7. Vorticity field in channel flow at $t = 100$: ——, computed; ∘, exact solution.

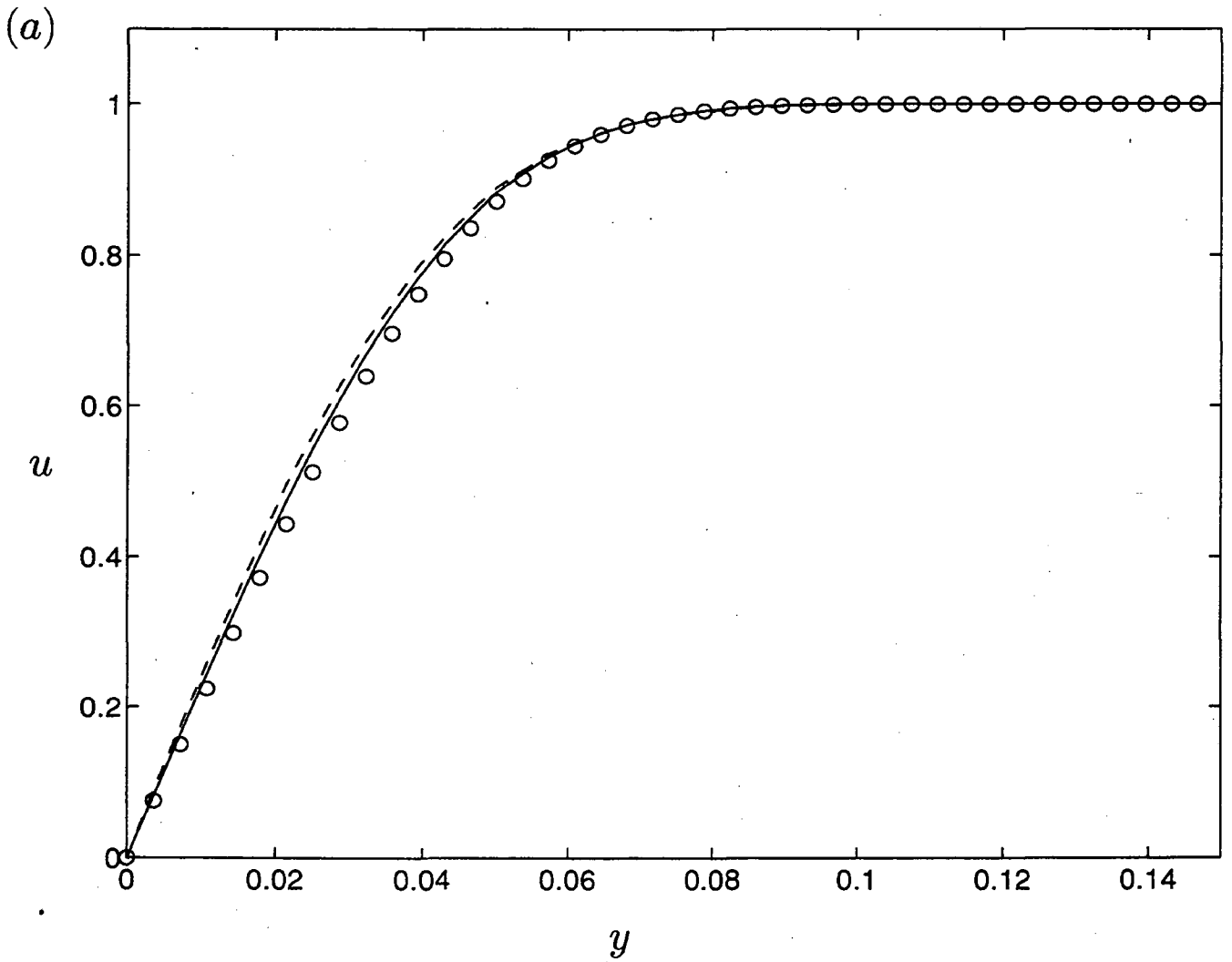

Fig. 8. Comparisons of u predictions in Blasius boundary layer: - - - -, $N = 1200$; ——, $N = 2700$; and $\circ$, Blasius solution. (a) $x = 2.5$, (b) $y = .05$.

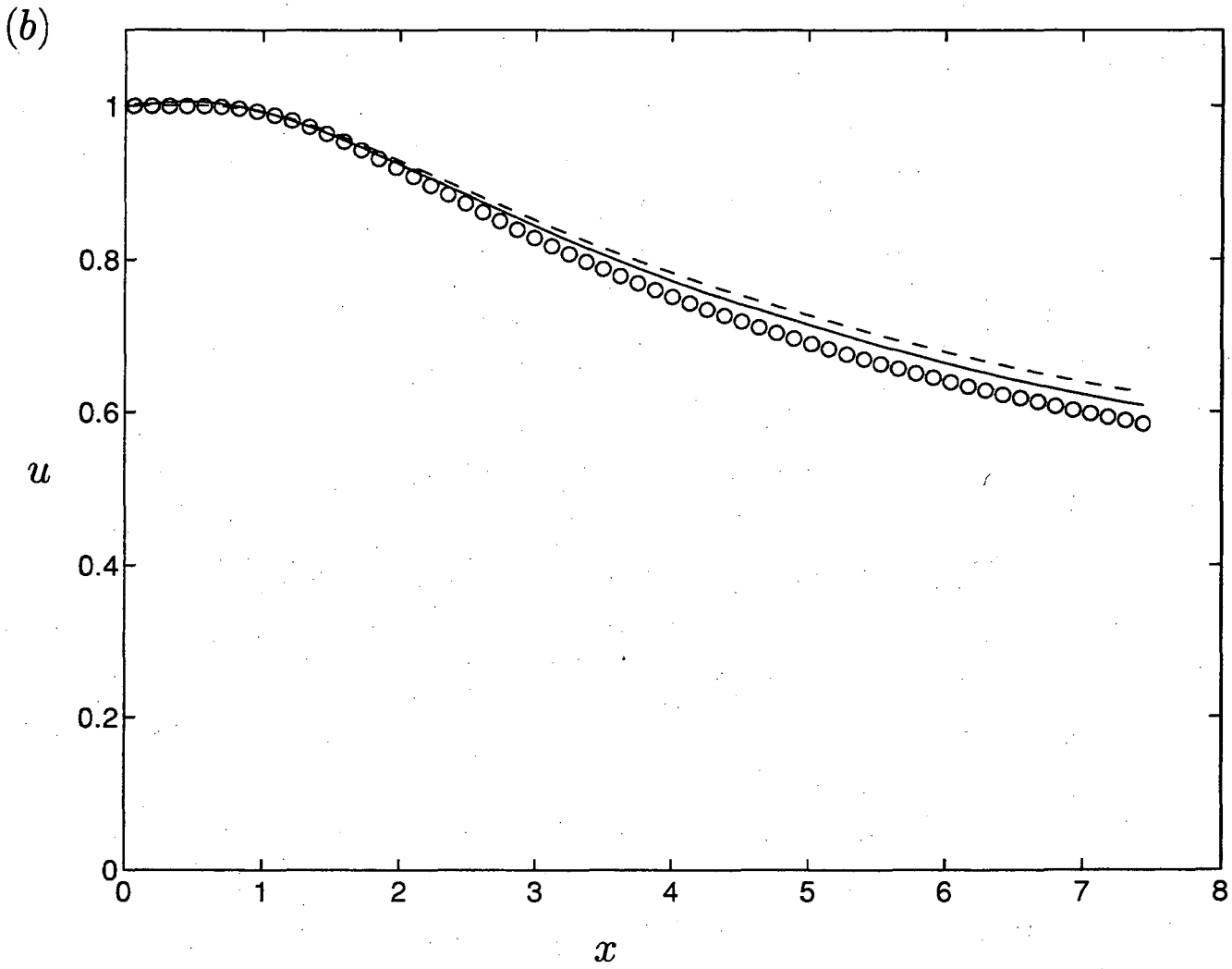

Fig. 8. Comparisons of u predictions in Blasius boundary layer: - - - -, $N = 1200$; ——, $N = 2700$; and $\circ$, Blasius solution. (a) $x = 2.5$, (b) $y = .05$.

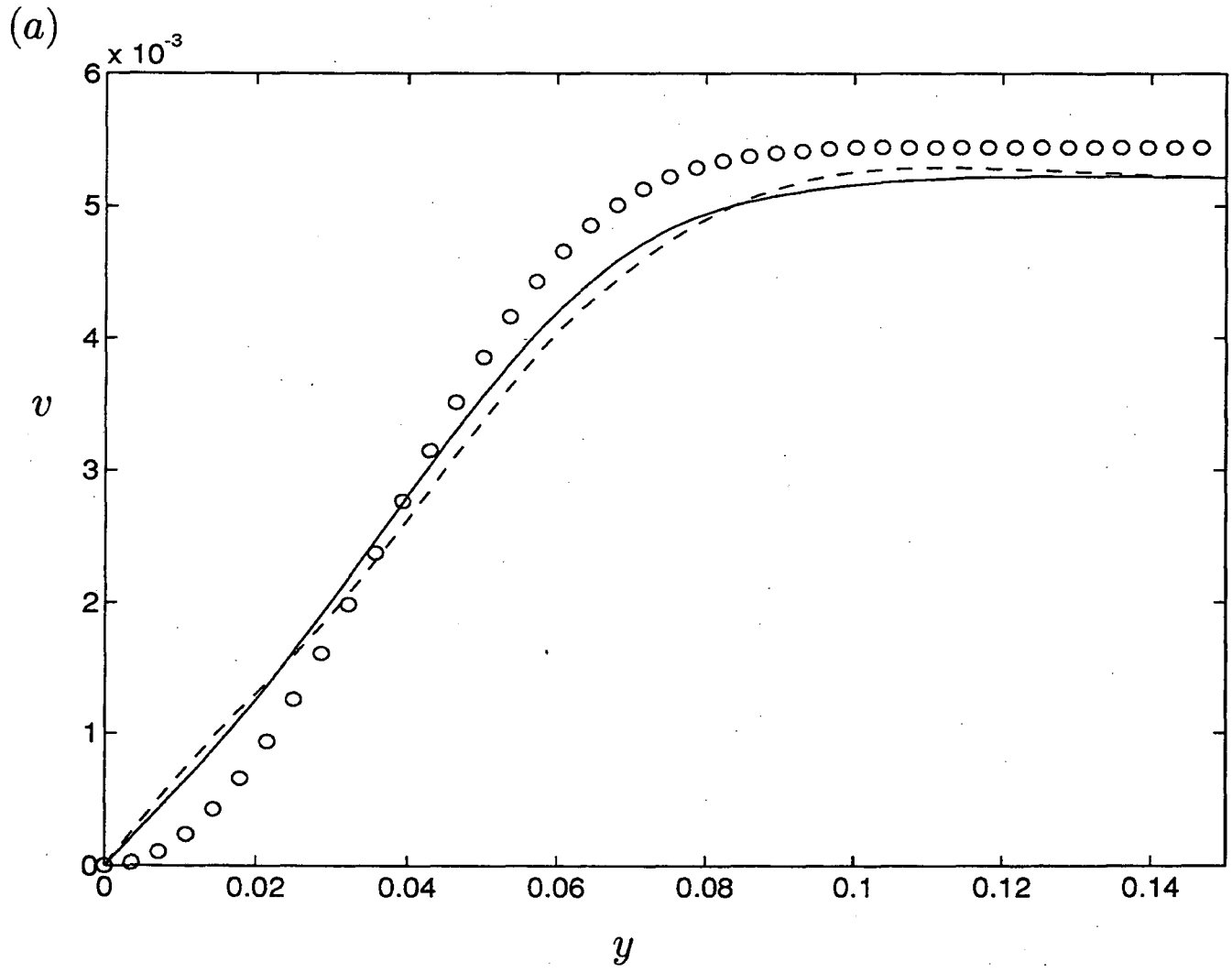

Fig. 9. Comparisons of v predictions in Blasius boundary layer: - - - -, $N = 1200$; ——, $N = 2700$; and $\circ$, Blasius solution. (a) $x = 2.5$, (b) $y = .05$.

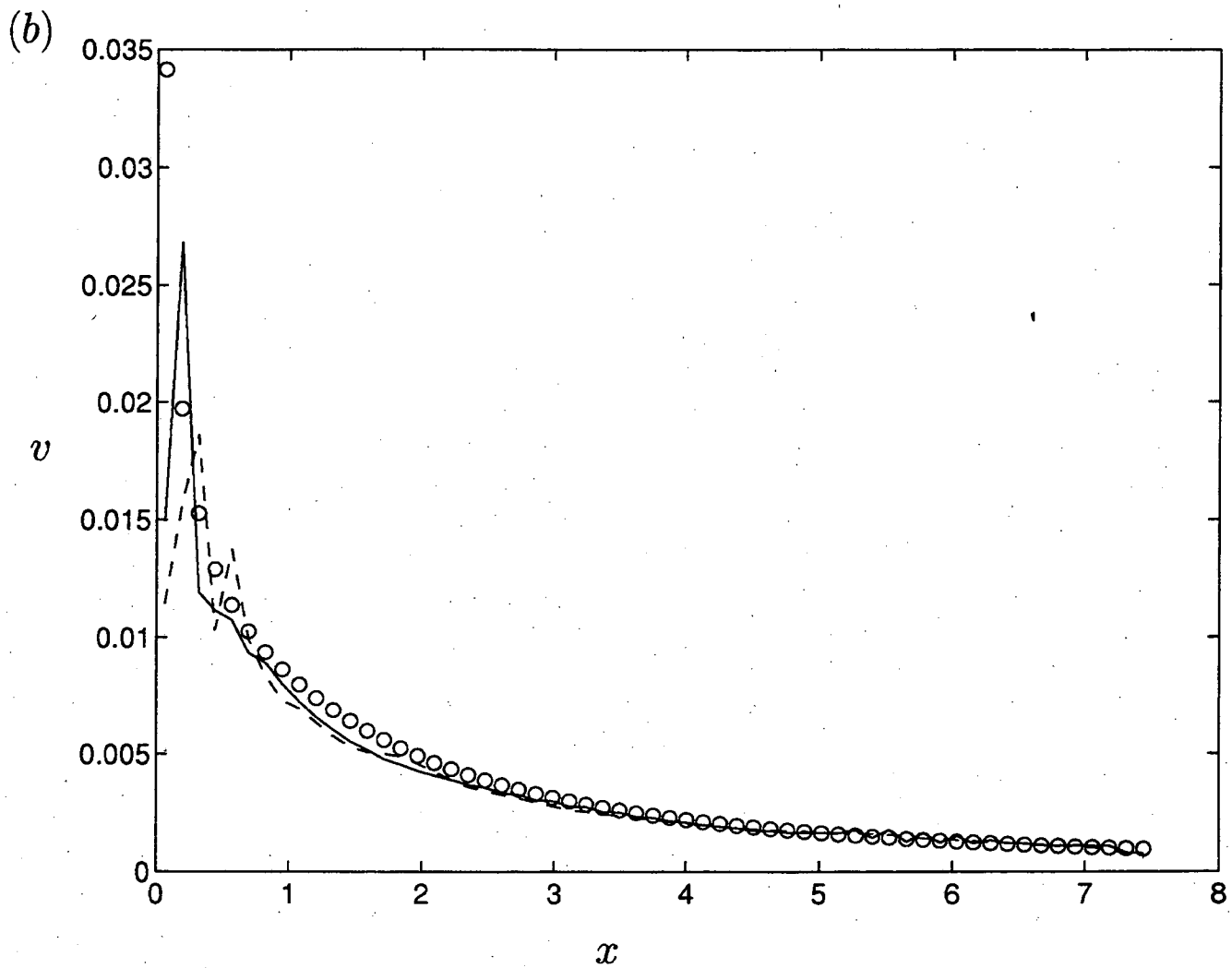

Fig. 9. Comparisons of v predictions in Blasius boundary layer: - - - -, $N = 1200$; ——, $N = 2700$; and $\circ$, Blasius solution. (a) $x = 2.5$, (b) $y = .05$.

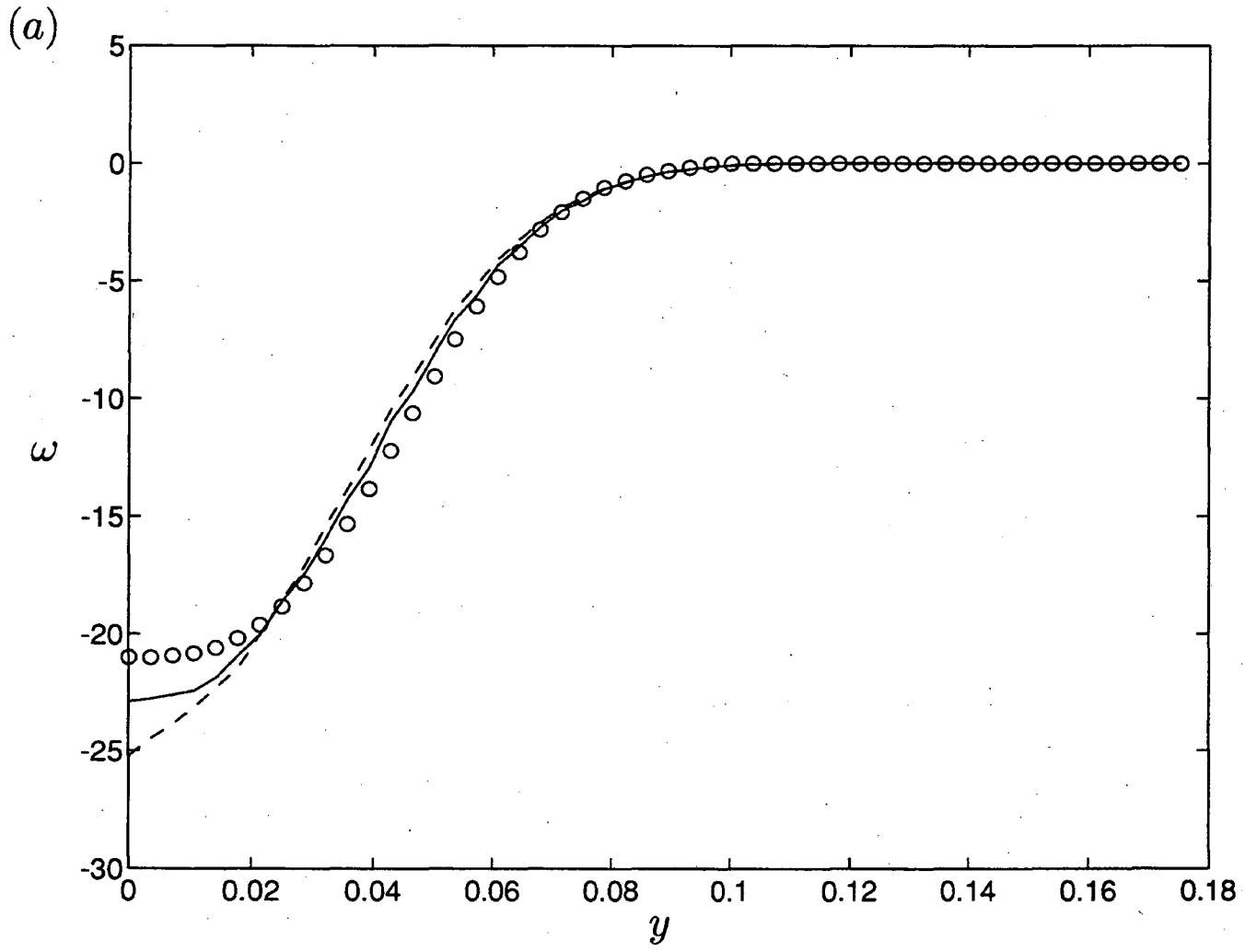

Fig. 10. Comparisons of ω predictions in Blasius boundary layer: - - - -, $N = 1200$; ——, $N = 2700$; and $\circ$, Blasius solution. (a) $x = 2.5$, (b) $y = 0$.

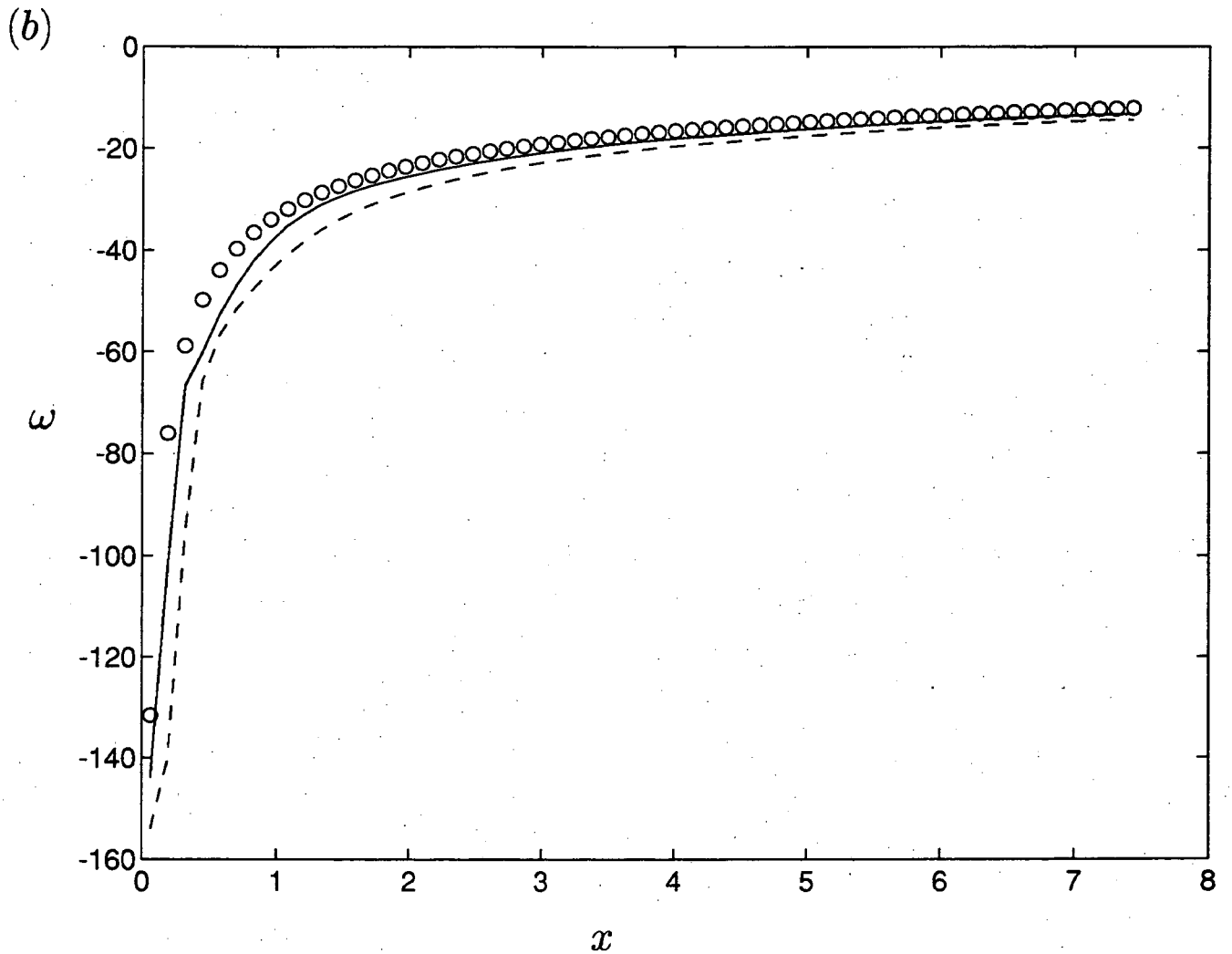

Fig. 10. Comparisons of ω predictions in Blasius boundary layer: - - - -, $N = 1200$; ——, $N = 2700$; and $\circ$, Blasius solution. (a) $x = 2.5$, (b) $y = 0$.

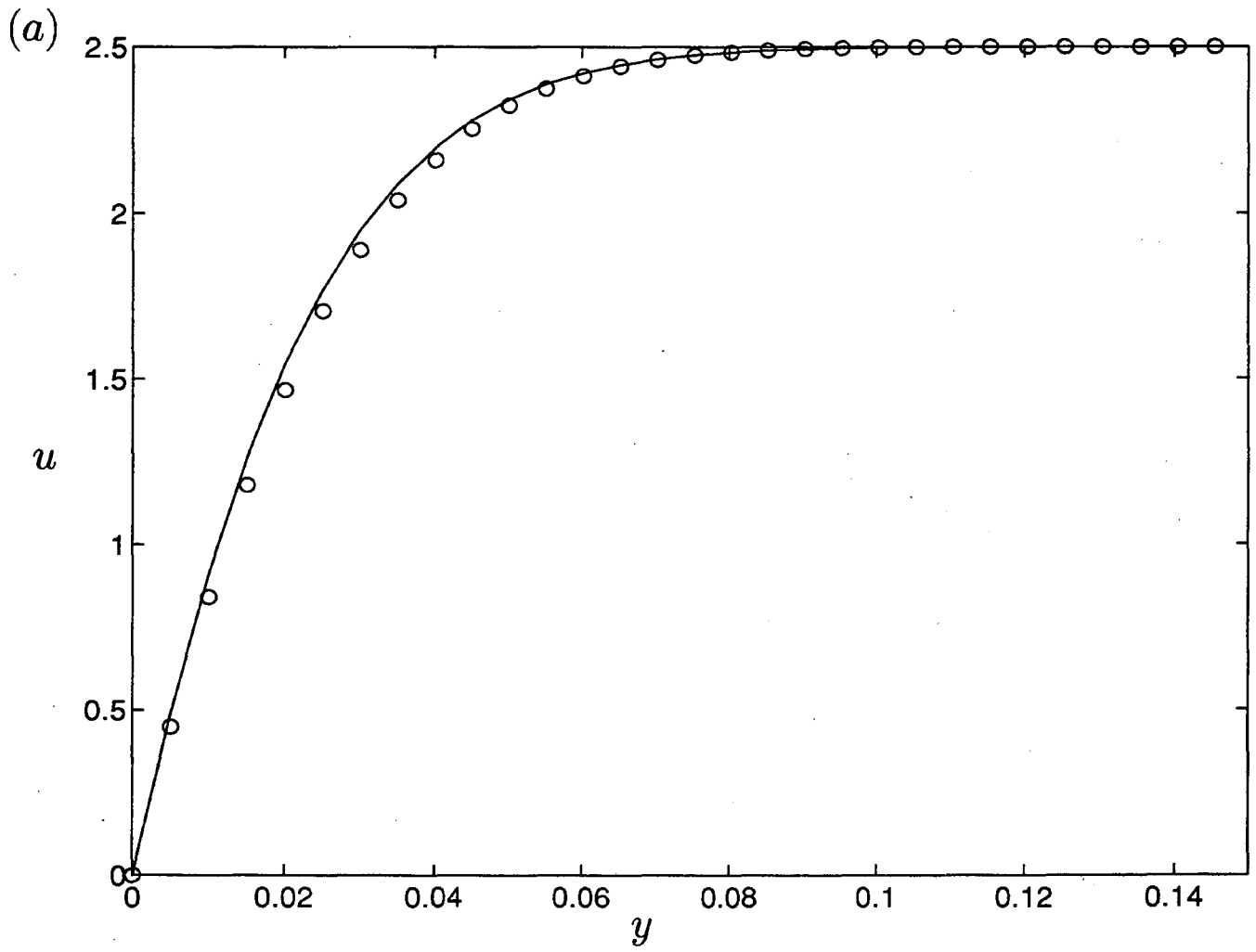

Fig. 11. Comparisons of u predictions in stagnation flow boundary layer: ——, computed; and ∘, Falkner-Skan solution. (a) $x = 2.5$, (b) $y = .1$.

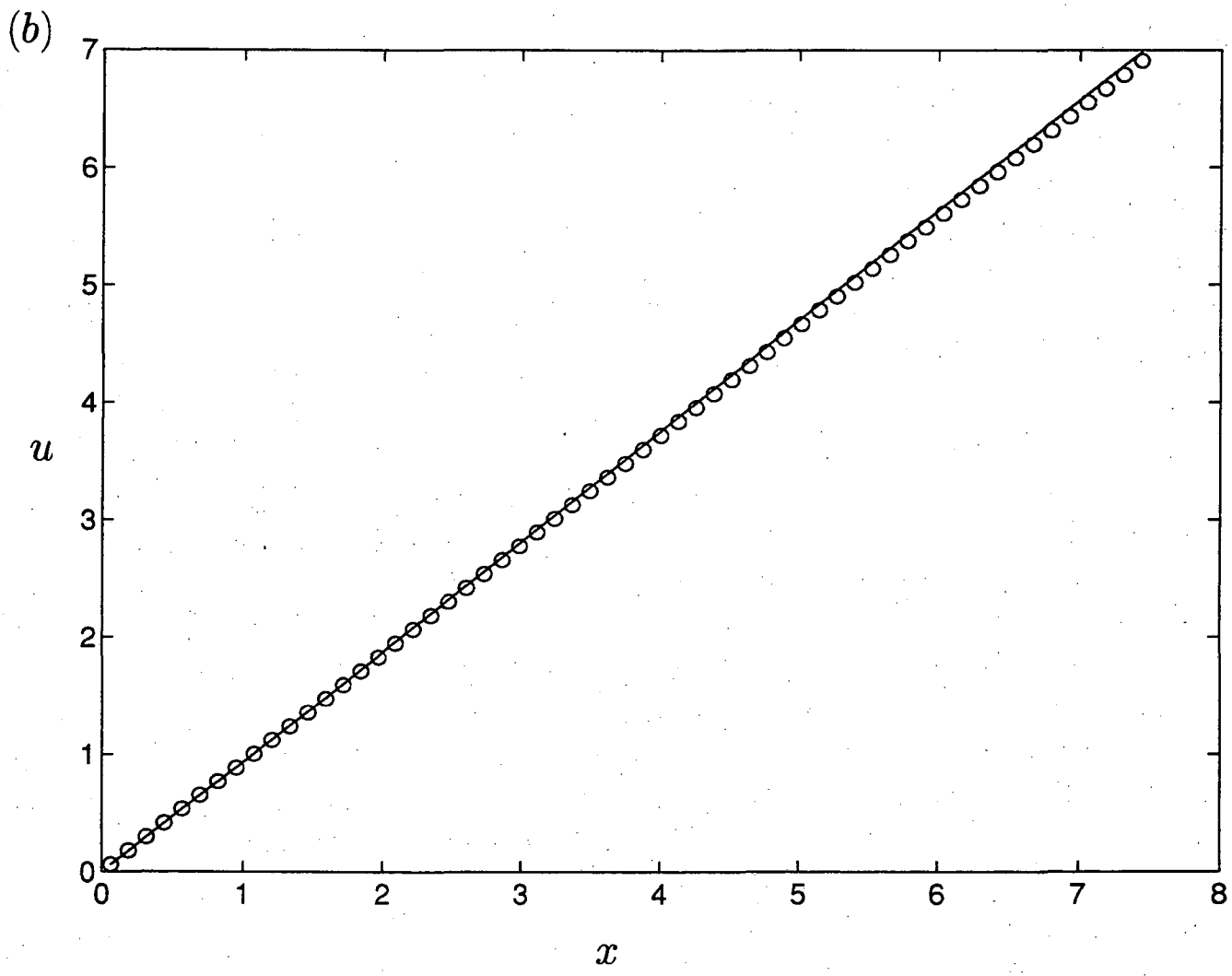

Fig. 11. Comparisons of u predictions in stagnation flow boundary layer: ——, computed; and ∘, Falkner-Skan solution. (a) $x = 2.5$, (b) $y = .1$.

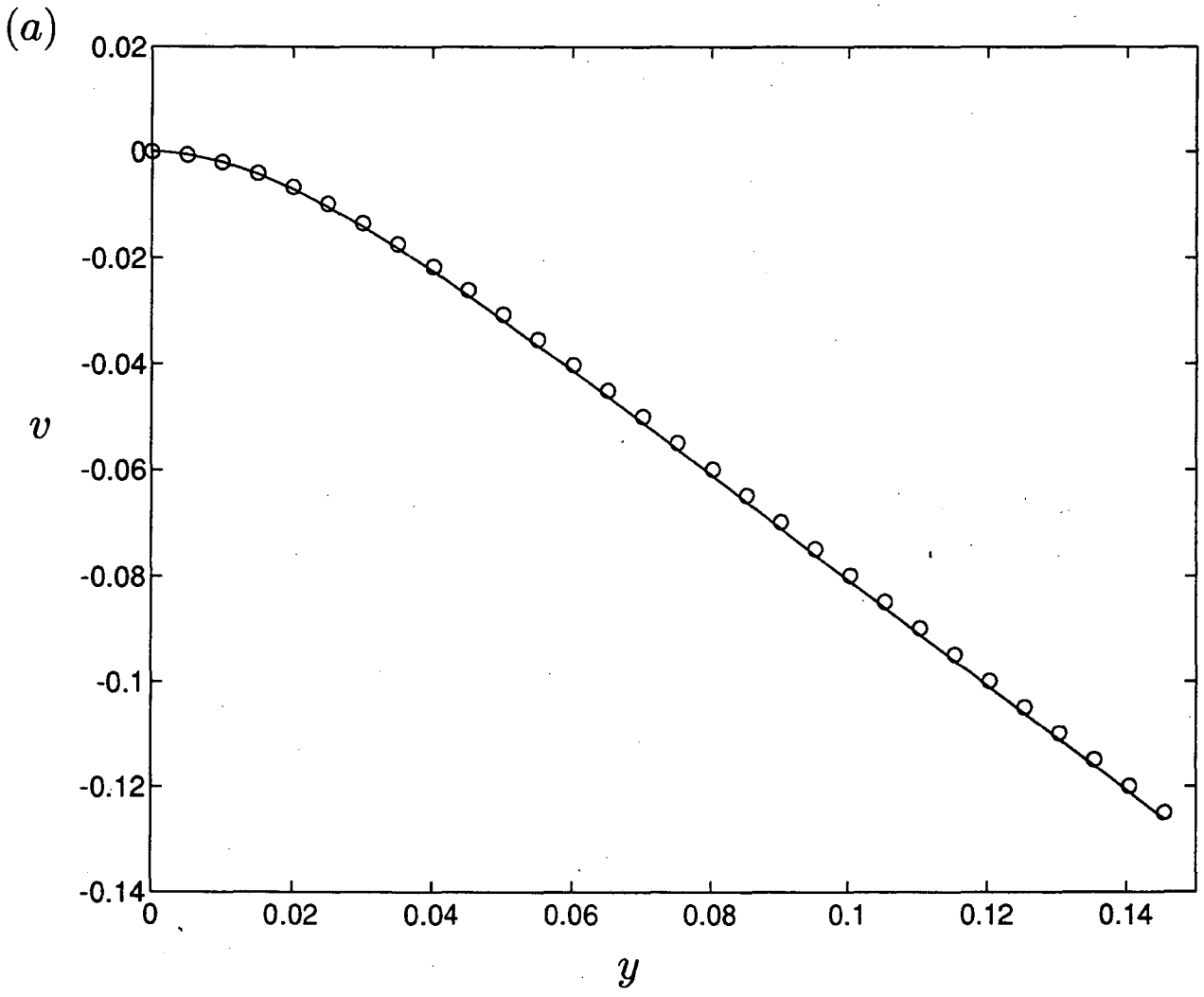

Fig. 12. Comparisons of v predictions in stagnation flow boundary layer: ——, computed; and ∘, Falkner-Skan solution. (a) $x = 2.5$, (b) $y = .1$.

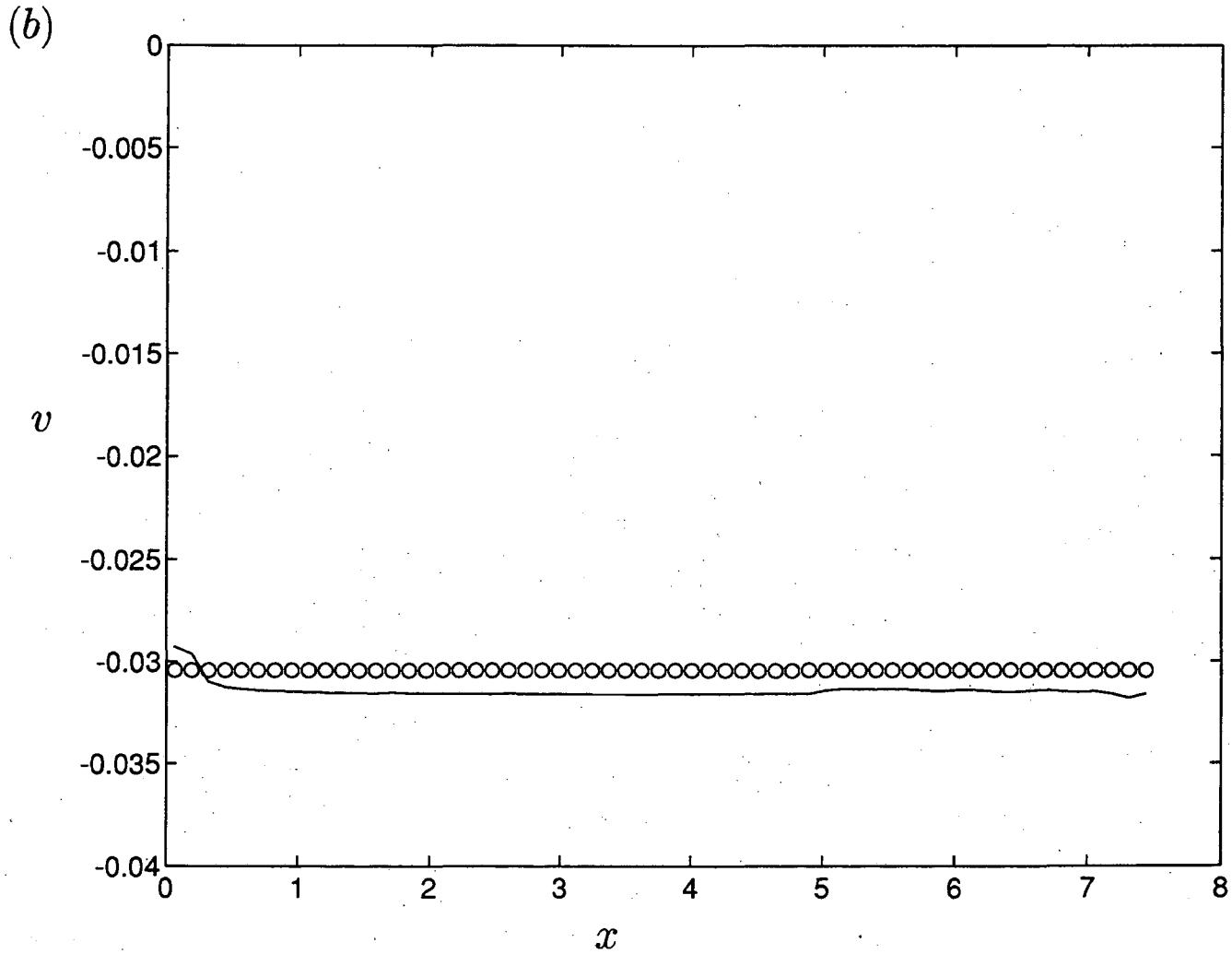

Fig. 12. Comparisons of v predictions in stagnation flow boundary layer: ——, computed; and ∘, Falkner-Skan solution. (a) $x = 2.5$, (b) $y = .1$.

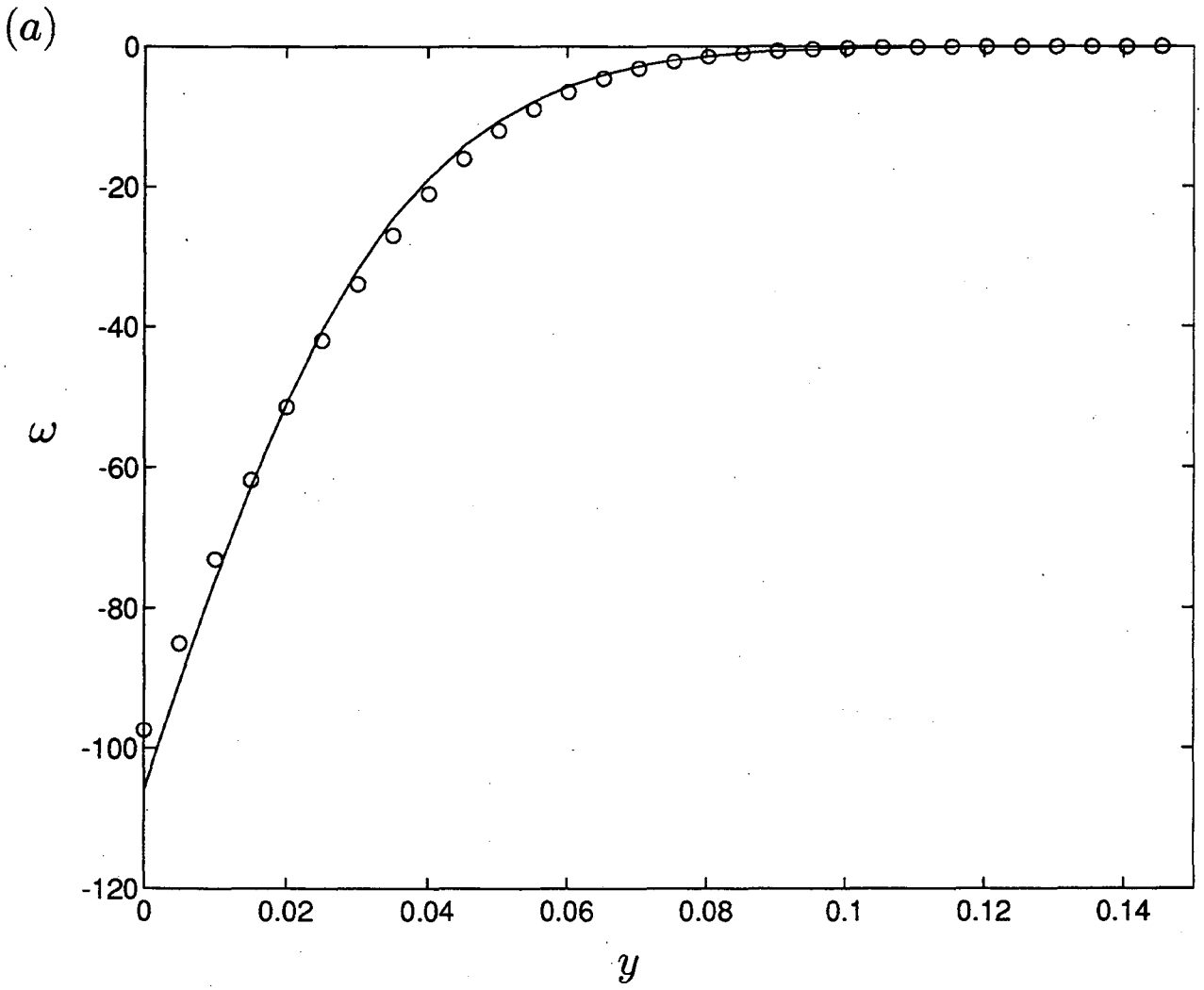

Fig. 13. Comparisons of ω predictions in stagnation flow boundary layer: ——, computed; and $\circ$, Falkner-Skan solution. (a) $x = 2.5$, (b) $y = 0$.

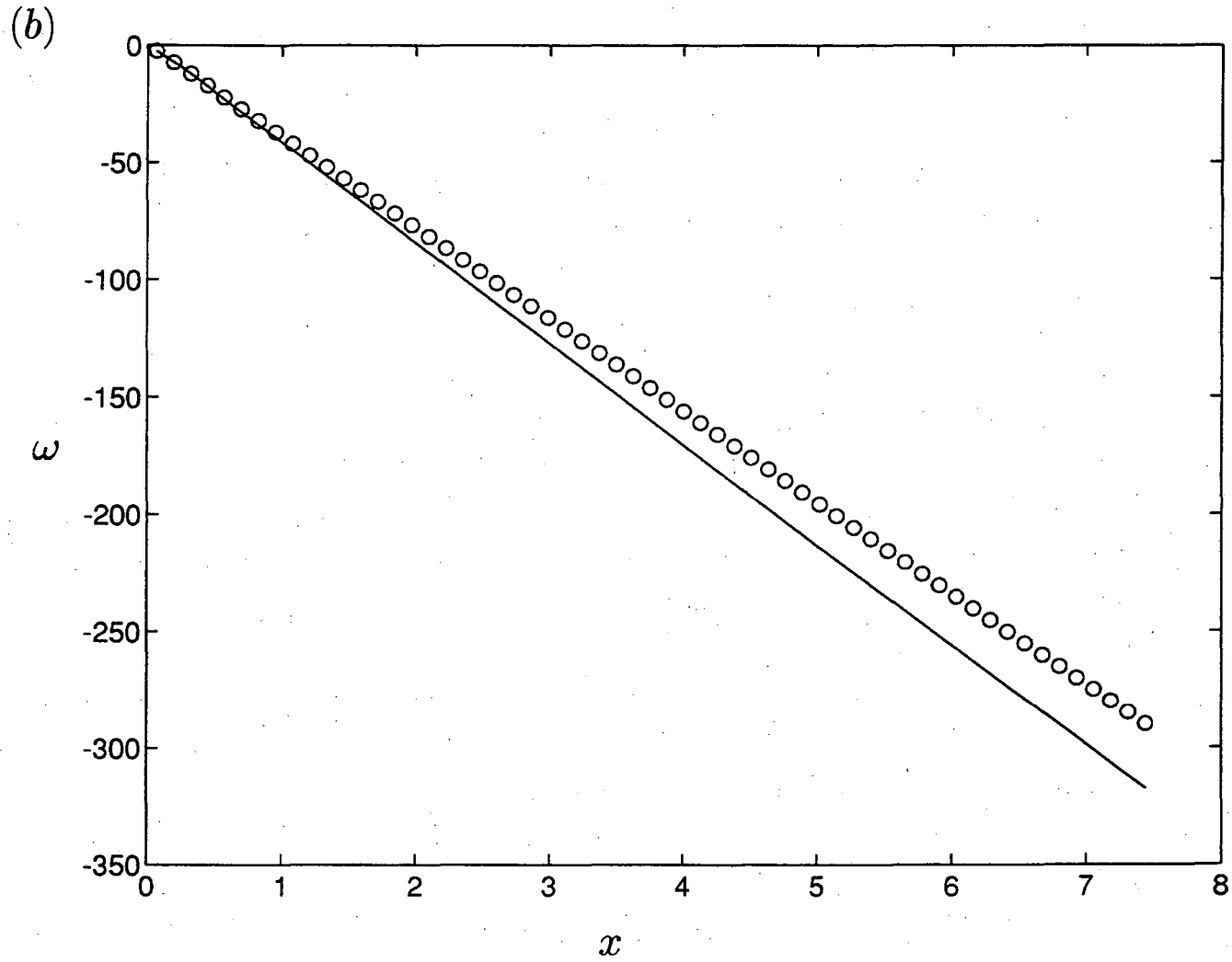

Fig. 13. Comparisons of ω predictions in stagnation flow boundary layer: ——, computed; and $\circ$, Falkner-Skan solution. (a) $x = 2.5$, (b) $y = 0$.

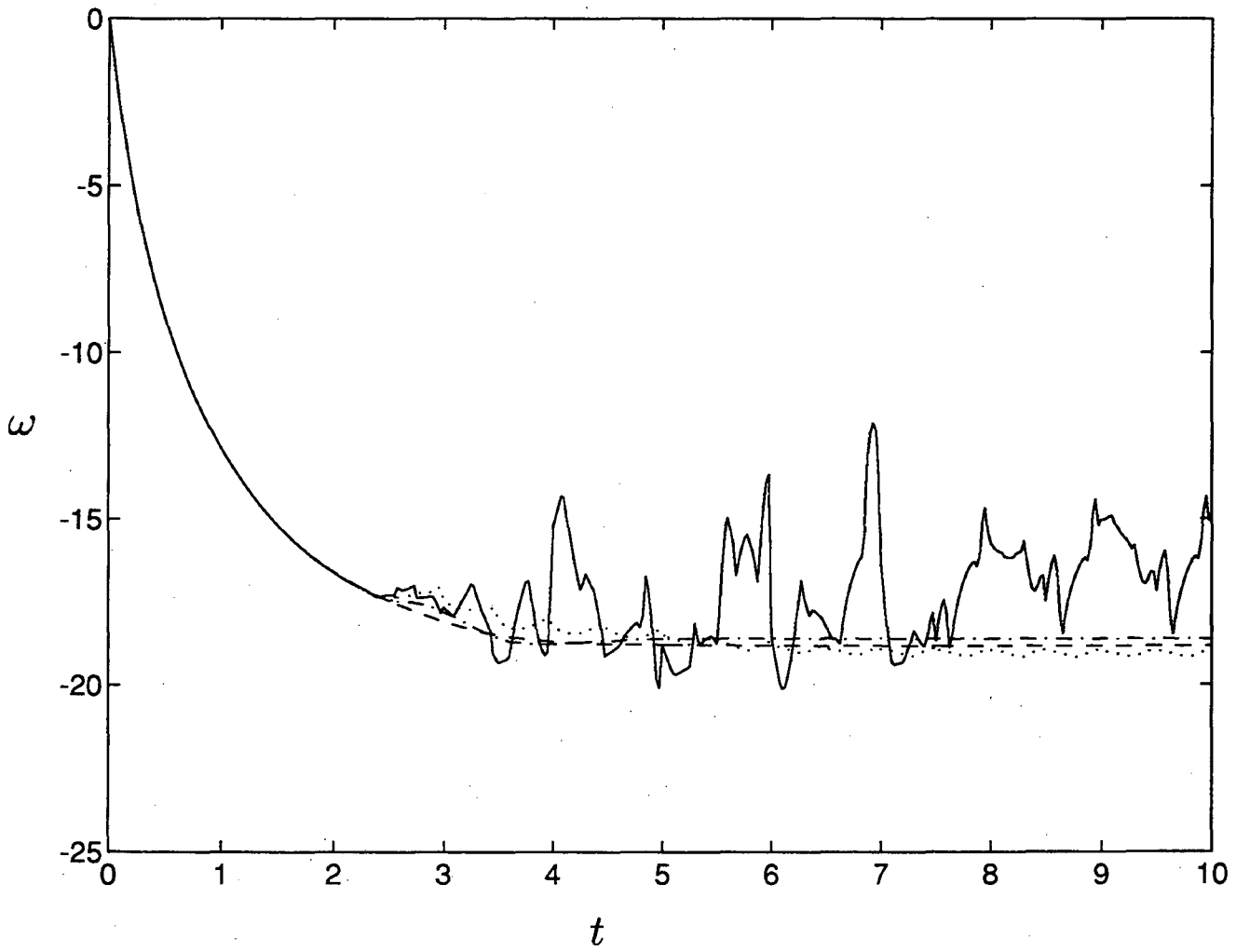

Fig. 14. Effect of t_{rs} on time record of ω at $x = 2.5, y = .025$ in a Blasius boundary layer. - - - -, $t_{rs} = .025$; - · -, $t_{rs} = .25$; · · ·, $t_{rs} = .50$; ——, $t_{rs} = 1$.

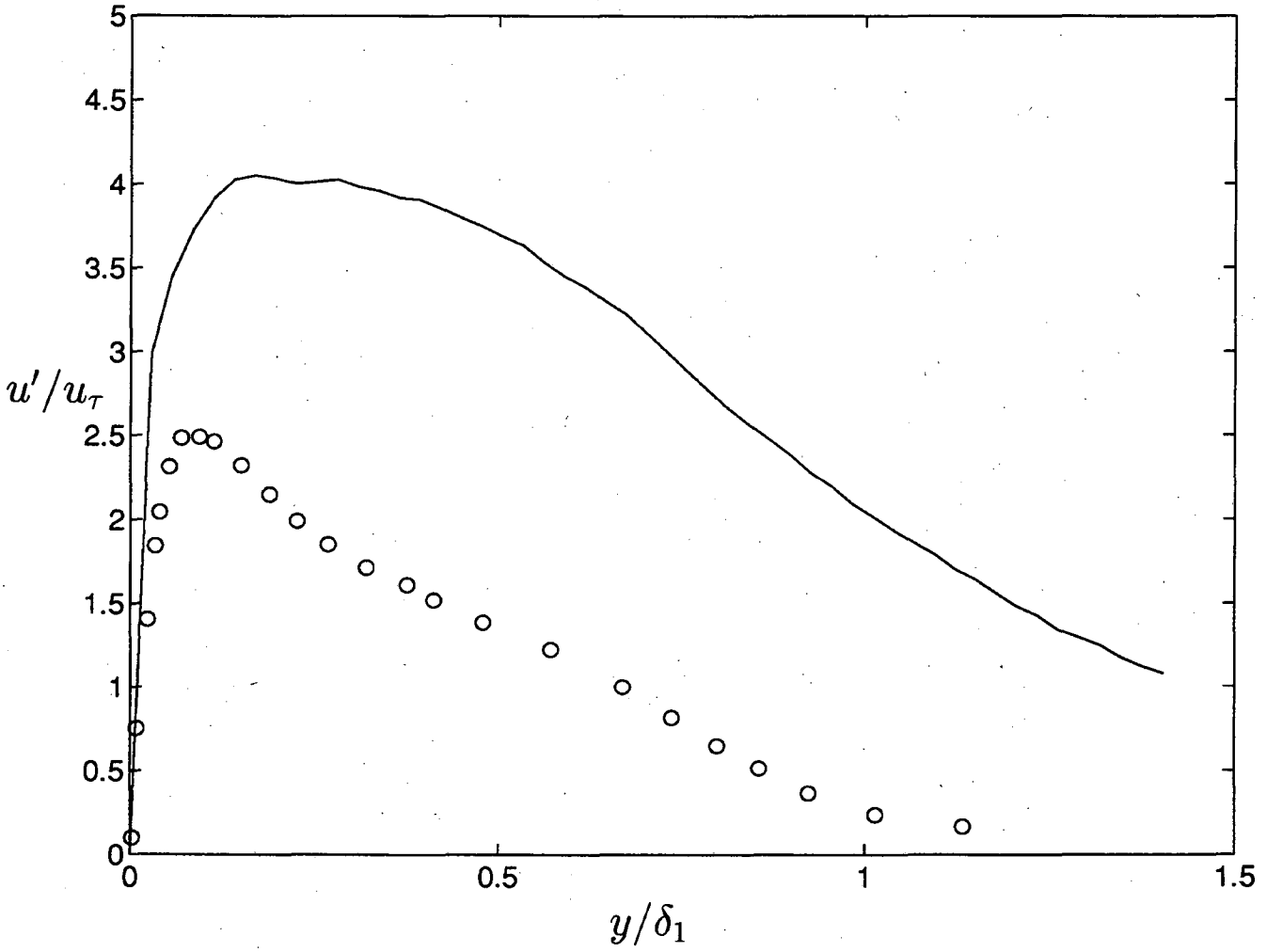

Fig. 15. u'/u_τ. ——, random sheet method; ∘, turbulent boundary layer in reference [24].

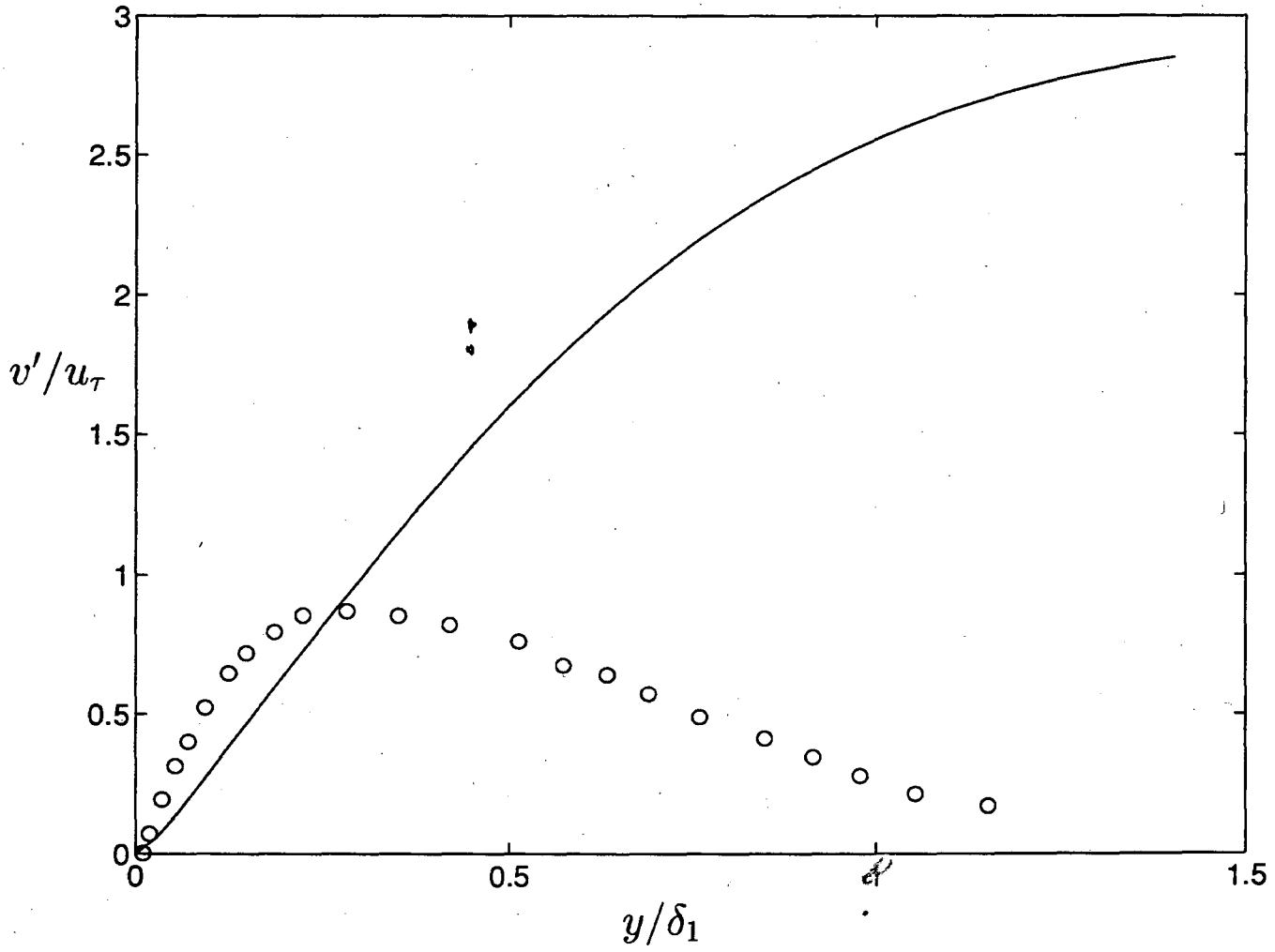

Fig. 16. v'/u_τ. ——, random sheet method; ∘, turbulent boundary layer in reference [24].

LAWRENCE BERKELEY LABORATORY
UNIVERSITY OF CALIFORNIA
TECHNICAL INFORMATION DEPARTMENT
BERKELEY, CALIFORNIA 94720

AAT220
LBL Libraries